Materials Science & Engineering A 772 (2020) 138821

Contents lists available at ScienceDirect

Materials Science & Engineering A

journal homepage: http://www.elsevier.com/locate/msea

Creep strength breakdown and microstructure in a 9%Cr steel with high B and low N contents

E. Tkachev *, A. Belyakov, R. Kaibyshev

Belgorod National Research University, Belgorod, 308015, Russia

ARTICLE INFO

Keywords:
Martensite
Steel
Microstructure
Precipitation
Characterization

ABSTRACT

A 9%Cr–3%Co steel with high B and low N contents exhibits creep strength breakdown at a temperature of 923 K after 3000 h. Specific feature of this steel is a distinct difference between short-term and long-term creep regimes for transient, steady state and tertiary creep stages. This behavior is unusual for high Cr steels and attributed to low density of $M_{23}C_6$ carbides precipitated on lath boundaries during tempering. Precipitation of Laves phase along these boundaries during transient creep followed by its coarsening affects significantly the creep mechanisms and results in the well-defined difference in mechanical behavior between the short- and long-term creep regimes. In contrast, the strain-induced formation of a small amount of Z-phase particles scarcely changes the creep behavior.

1. Introduction

Deterioration of the creep strength has been frequently observed in advanced 9–12%Cr creep resistant steels [1–7]. This degradation in the creep resistance is associated with a drastic change of the relatively weak rupture time dependence of the creep strength inherent in short-term creep to a rapid decrease in the creep strength with an increase in the rupture time during long-term creep and has been termed as the creep strength breakdown [5–7]. The creep strength breakdown results in the progressive decrease in allowable stress with increasing service period [1–7]. Unfortunately, origin of this phenomenon is still unclear. It is obvious that the degradation of initial tempered martensite lath structure (TMLS), which consists of a hierarchical microstructure with prior austenite grains (PAG) subdivided into martensite packets, blocks, and laths [1,14], upon creep plays an important role in the deterioration of the creep strength during long-term creep [6–13]. The change in TMLS during creep occurs in two sequential processes [7,9,10,15,16]. First, the lath boundaries, which are irregular dislocation network exerting high internal stresses [17], evolve to subboundaries, which are regular dislocation network with low internal stresses. This evolution process is assisted by knitting reactions between lattice dislocations and dislocations composing lath boundaries, relieving internal stresses. Second, the migration of subboundaries over large distances leads to replacement of lath-type structure by coarse subgrain structure owing to subboundary coalescence, which is accompanied by a decrease in dislocation density [7,9,10,15,16]. The lath-type structure was retained up to fracture upon the short-term creep, whereas the coarse subgrains were observed in the ruptured specimens after long-term creep [6,7,9].

The degradation of TMLS has been attributed to coarsening of dispersoids, which should impede the knitting reactions and exert a high Zener drag pressure [4–24]. Three types of secondary phases generally stabilize TMLS under long-term aging and creep. First, a portion of $M_{23}C_6$ carbides with an average size of approx. 100 nm precipitates during tempering on lath boundaries [1,7–13,15,16]. These precipitations delay the dislocation knitting reaction [17,25] and prevent the migration of lath boundaries [7,11,12,15,16,26,27]. Second, uniformly distributed (Nb,V)(C,N) particles (say MX carbonitrides) with an average size of 10–50 nm develop during tempering [1–3,5–13,28,29]. Two-phase separation of the MX particles into V-rich and Nb-rich particles provides their high coarsening resistance during creep at elevated temperatures [1,7,10,15,16,28,29]. These dispersoids hinder the movement of lattice dislocations and impede the knitting reactions in the lath boundaries [10,15–17,25]. Third, precipitation of some Laves phase particles during aging or creep on the lath boundaries hinders both the knitting reaction and the migration of subgrain boundaries [1,7,10–12,15,16,25,30–32]. In addition, these particles strengthen the steel during transient creep [20]. It is worth noting that $M_{23}C_6$ and Laves phase particles, which develop on high-angle boundaries (HAB) of hierarchical microstructure are larger than those precipitated on

* Corresponding author. Belgorod National Research University, Pobeda 85, Belgorod, 308015, Russia.
E-mail address: tkachev_e@bsu.edu.ru (E. Tkachev).

https://doi.org/10.1016/j.msea.2019.138821
Received 25 October 2019; Received in revised form 10 December 2019; Accepted 11 December 2019
Available online 13 December 2019

Table 1
Chemical composition of the studied steel (wt.%).

C	Si	Mn	Cr	W	Mo	Nb	V	Co	Ni	Cu	Ti	Al	N	B	Fe
0.1	0.12	0.4	9	1.5	0.57	0.05	0.2	2.8	0.24	0.027	0.002	0.01	0.007	0.012	Bal.

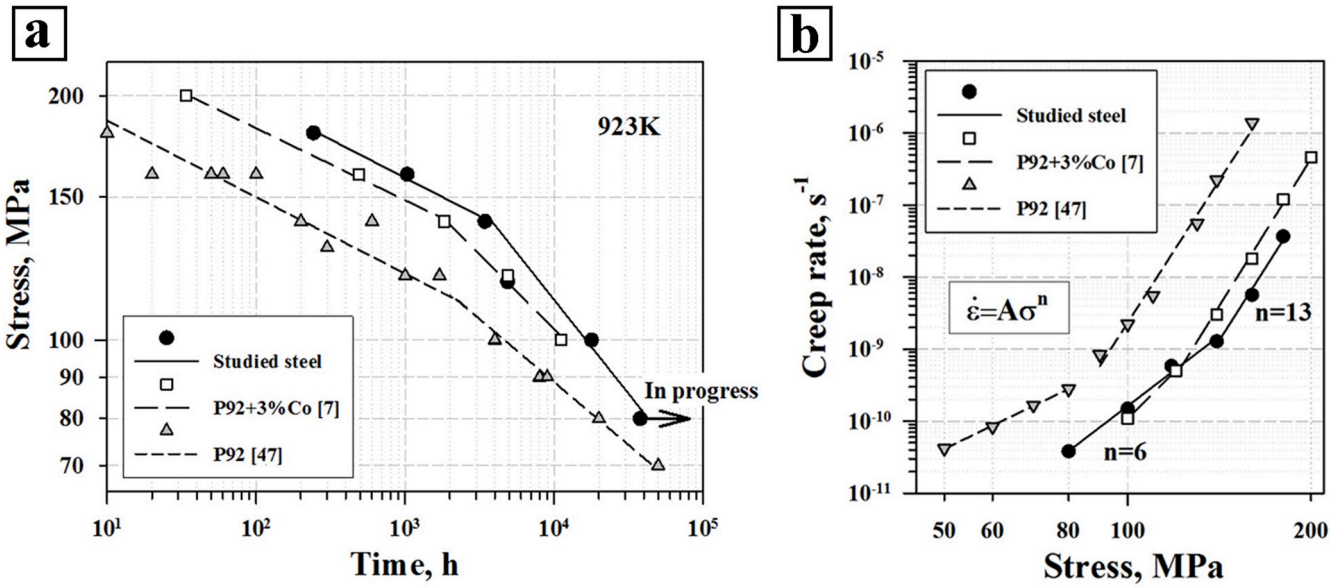

Fig. 1. Creep rupture strength (a) and stress dependence of minimum creep rate (b) of the studied and some other high-Cr steels at 923K [7,47].

low-angle boundaries (LAB) [11,12,32]. Under long-term aging and creep the coarsening of relatively large $M_{23}C_6$ carbide and Laves phase particles leads to dissolution of fine particles precipitated on lath boundaries in accordance with Gibbs-Thomson relationship [7,10,11,17,22–26,33]. The strain-induced coarsening is extremely important for dissolution of $M_{23}C_6$ carbides precipitated on lath boundaries, while the deformation effect on coarsening of Laves phase particles is not obvious [7,15,16].

The creep strength breakdown depends on chemical composition of high Cr steels. In P91/P92 type steels containing 0.1%C and 0.05%N, the creep strength breakdown correlates with W removal from the solid solution [7]. This solid solution depletion accelerates diffusion within ferritic matrix and hastens the coarsening of $M_{23}C_6$ carbides [7,10.16]. The creep strength breakdown took place as the pinning pressures decreased below a critical value of about 0.08 MPa, when the lath structure completely transformed to subgrain one [7]. The creep strength breakdown in 11%Cr steels of P122 type is associated with the replacement of nanoscale MX carbonitrides by coarse Z-phase particles (CrVN) [14,18–21]. The Z-phase particles exhibit relatively high coarsening rate under creep at elevated temperatures as compared to other precipitates and, thus, are considered as undesirable from the standpoint of microstructural stability [23,24,34].

An increase in boron and a decrease in nitrogen contents made it possible to reduce the coarsening rate of $M_{23}C_6$ carbides due to a replacement of carbon by boron in these carbides. Thus, two-phase separation to B-free $M_{23}C_6$ carbides and $M_{23}(B{\cdot}C)_6$ phase slows down the degradation of the microstructure, thereby, increasing the creep resistance [10,15,16,35–40]. Nitrogen content is reduced to avoid the formation of boron nitride (BN) and to suppress the formation of undesirable Z-phase during creep. The relatively stable carbides, in turn, stabilize the TMLS under creep at elevated temperatures, enhancing the creep resistance [10,15,16,39–42]. In spite of certain achievements in the elaboration of this alloying design for martensitic/ferritic heat resistant steels, the origin of the creep strength breakdown in advanced steels belonging to P93 type is still unclear [10,15,16,35,36,38,43–46].

The aim of the present study is to assess the effect of microstructural changes on the creep behavior of an advanced heat resistant steel. The changes in TMLS and dispersed particles are comparatively investigated during creep and aging in order to reveal the physical mechanisms controlling the transition from short-term creep to long-term one.

2. Experimental

The chemical composition of the studied steel is given in Table 1. The steel was produced by vacuum induction melting followed by solution treatment at 1423 K and, then, hot forging in the temperature interval of 1423 K ÷ 1273 K. The steel was heated to 1333 K for 0.5 h, air cooled and, then, tempered at 1023 K for 3 h. The specimens of 7 × 3 mm^2 in cross section and 25 mm in gauge length were crept at 923 K in air under initial loads of 180, 160, 140, 118 and 100 MPa using ATS2330 lever arm machines. The hardness in the grip and gauge (within uniform elongation) portions of crept specimens was measured using the Brinell hardness testing under a load of 750 N. Vickers test with a load of 50 g and a holding time of 10 s was used to examine hardness near fracture surface of ruptured specimens.

The microstructural investigations of all ruptured specimens were performed in the longitudinal sections by Quanta 600 FEG scanning electron microscope (SEM) incorporating an orientation imaging microscopy (OIM) system and transmission electron microscopy (TEM) using a JEM-2100 microscope operating at 200 kV equipped with an INCA energy-dispersive X-ray spectrometer. The methods of energy dispersive analysis and selected area diffraction (SAD) were used to distinguish different phases and to characterize the precipitates in the specimens. The TEM specimens were electro-polished with perchloric acid (10%) and glacial acetic acid (90%) under a voltage of 22.5 V at ambient temperature. The transverse lath/subgrain sizes were

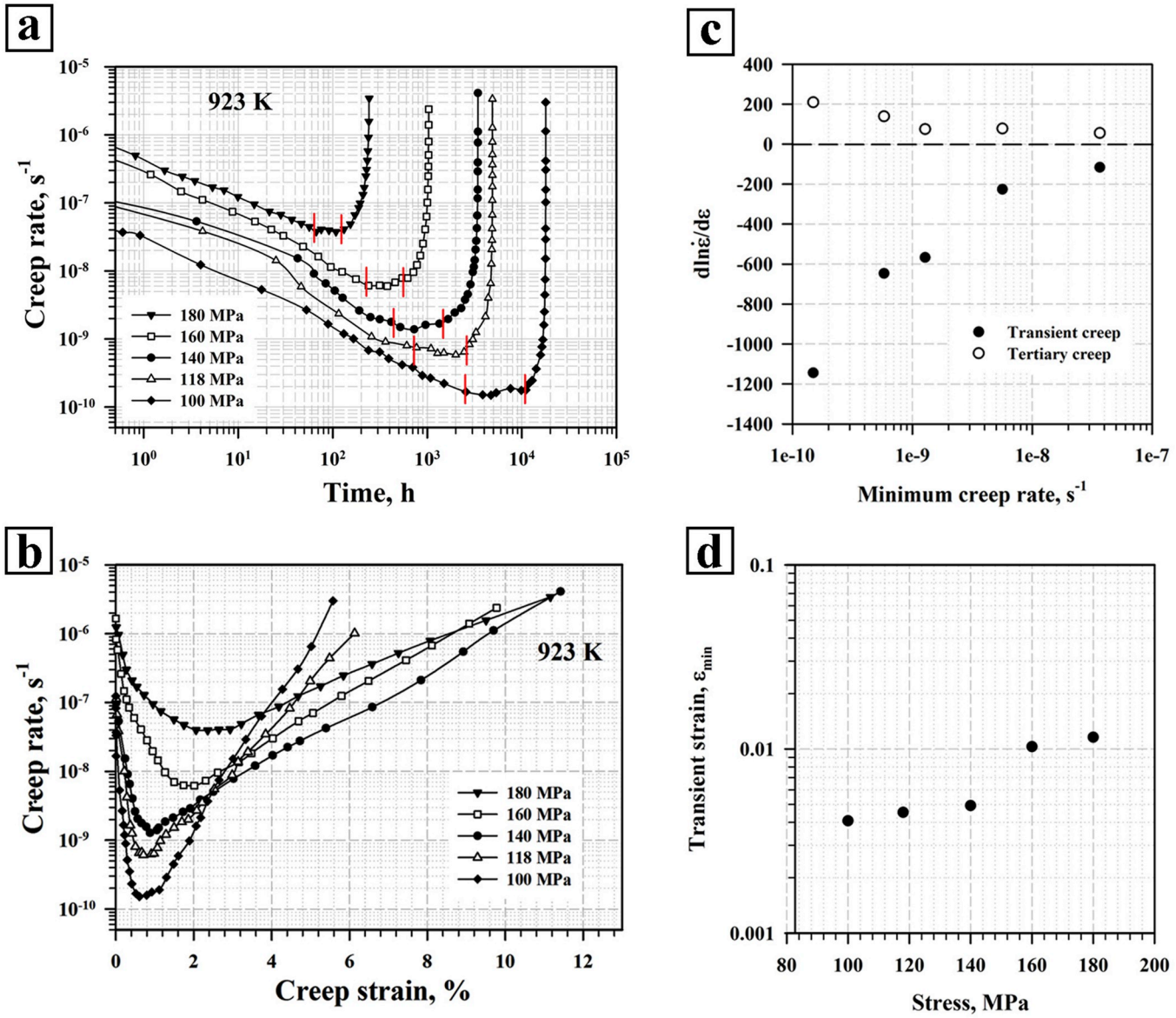

Fig. 2. Creep rate vs time (a), creep rate vs strain (b), effect of applied stress on $d\ln\dot{\varepsilon}/d\varepsilon$ values for transient and tertiary creep stages (c), and dependence of transient strain, ε_{min}, on applied stress (d).

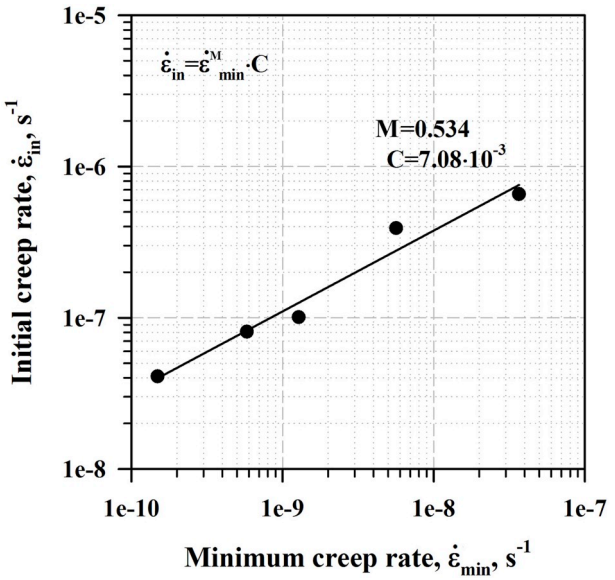

Fig. 3. Relationship between the initial creep rate and the minimum/steady-state creep rate.

calculated by a linear intercept method, taking into account all observed (sub)boundaries on typical TEM images. Extraction carbon replicas of etched samples were prepared to evaluate the size and chemical composition of second phase particles. The mean sizes of investigated precipitates were quantitatively determined as an average of the short and long intercepts. At least 100 individual particles were measured for each type of precipitates (except the Z-phase) per each data point. The dislocation densities were evaluated as a number of individual dislocations crossing a unit area inside the lath/subgrain using at least ten arbitrarily selected typical TEM images obtained under multiple beam contrast condition. Volume fractions of precipitates were calculated by the ThermoCalc software with TCFE7 database.

3. Results

3.1. Creep behavior

The creep rupture strength of the studied steel is shown in Fig. 1a along with those for P92 and P92 + 3%Co steels [7]. The time to rupture, t_r, of the studied steel is significantly longer than that of P92 type steels. The creep strength breakdown, which can be recognized as a deflection point in Fig. 1a of the present steel and the P92 + 3%Co steel is observed at the same stresses of 140 MPa, which is higher than that for the P92 steel (110 MPa). The time to rupture of the studied steel, at which the creep strength breakdown appears, is twice that of P92 and P92 + 3%Co steels. In contrast to the P92 steel [7,47], the creep strength breakdown in Fig. 1a clear correlates with the power-law creep breakdown in Fig. 1b when the stress exponent (n) drastically changes from 13 to 6. Therefore, the deformation mechanism controlling the steady-state creep changes at the creep strength breakdown. The stress exponent of 6 in the range of long-term creep is typical for warm deformation, when the rearrangement of dislocations by low temperature climb controlled by pipe diffusion occurs. The relatively high value of n = 13 in the range of short-term creep can be attributed to the suppression of diffusion-controlled dislocation rearrangements [48,50].

The strain dependence of creep rate can be expressed as follows [45,49].

$$\dot{\varepsilon} \sim \dot{\varepsilon}_0 \exp(n\varepsilon)\exp(m\varepsilon)\exp(d\varepsilon)\exp(i\varepsilon), \quad (1)$$

$$d \ln\dot{\varepsilon} / \varepsilon = n + m + d + i \quad (2)$$

where $\dot{\varepsilon}_0$ is the initial creep rate, m is the parameter of degradation of TMLS, d is the damage parameter attributed to strain or diffusion-induced cavitations, and i describes the effect of necking. Parameter n in Eqs. (1) and (2) corresponds to the stress exponent in power-law creep rate relationship [48,50]:

$$\dot{\varepsilon}_{ss} = A\cdot\sigma^n \exp\left(\frac{-Q}{RT}\right), \quad (3)$$

where, $\dot{\varepsilon}_{ss}$ is the steady-state creep rate, which can be replaced by the minimal creep rate value ($\dot{\varepsilon}_{min}$), A is a constant, σ is the applied stress, Q is the activation energy for plastic deformation, R is the gas constant and T is the absolute temperature. The transient creep behavior can be described by an empirical relationship as suggested by Garofalo [15,51]:

$$\varepsilon = \varepsilon_0 + \varepsilon_T[1 - \exp(-r^{'}\cdot t)] + \dot{\varepsilon}_{min}\cdot t, \quad (4)$$

where ε_0 is the instantaneous strain on loading, r' is the rate of exhaustion of transient creep, t is time, and ε_T is the transient creep strain. The concept of the rearrangement of dislocations into a stable configuration over the relaxation time (τ) during transient creep was invoked to provide a physical understanding of Eq. (4) [50]. In this concept, the first-order reaction-rate kinetics is described as follows [15,51]:

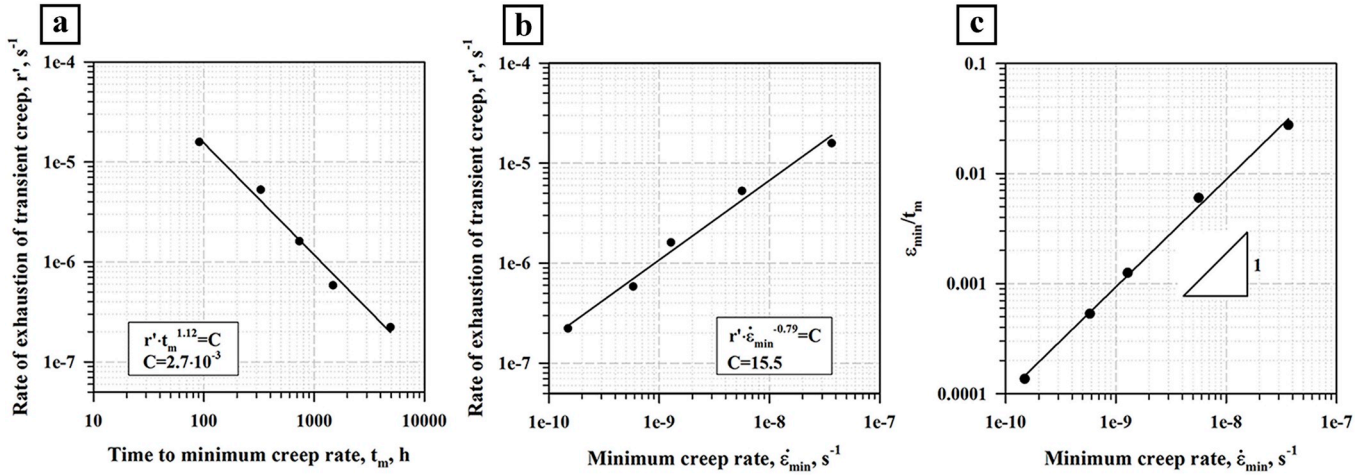

Fig. 4. Variation of the rate of exhaustion of transient creep, r', with the offset time, t_m, (a) and the minimum/steady-state creep rate, $\dot{\varepsilon}_{min}$ (b), and the relationship between the minimum/steady-state creep rate, $\dot{\varepsilon}_{min}$, and ε_{min}/t_m (c).

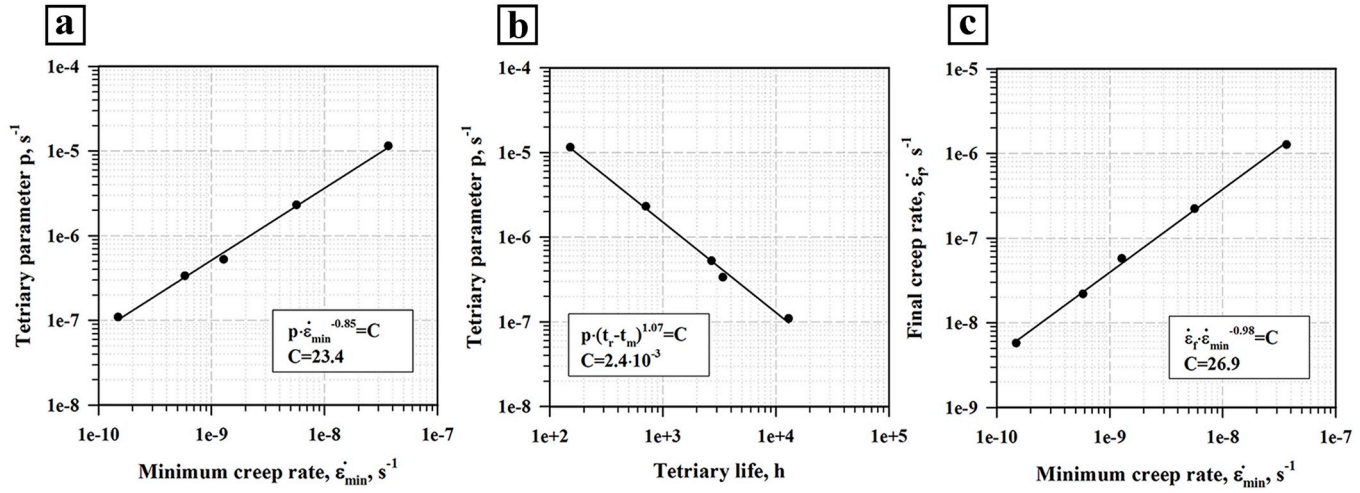

Fig. 5. Variation of the rate of acceleration of tertiary creep, p, with minimum/steady-state creep rate (a), the dependence of the rate of acceleration of tertiary creep on time in tertiary stage, (t_r-t_t), (b), and the dependence between the final creep rate, $\dot{\varepsilon}_f$, and the minimum/steady-state creep rate, $\dot{\varepsilon}_{min}$, (d).

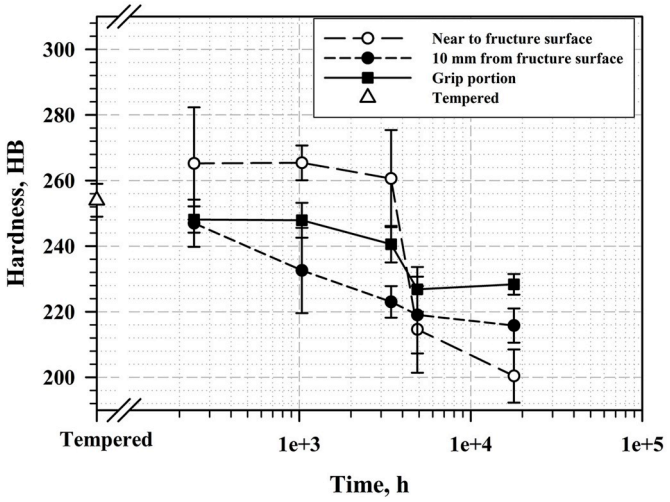

Fig. 6. Effect of aging/creep time on hardness in different portions of the crept specimens.

$$\frac{d\dot{\varepsilon}}{dt} = \frac{-(\dot{\varepsilon} - \dot{\varepsilon}_{min})}{\tau}, \tag{5}$$

For Eqs. (4) and (5), the following dependence is fulfilled, $1/\tau = r' = K \times \dot{\varepsilon}_{ss}$, where K is a constant [51].

The creep rate vs time/strain curves are shown in Fig. 2a–b, respectively, and the effect of applied stress on the $d\ln\dot{\varepsilon}/\varepsilon$ parameter is shown in Fig. 2c. The linear dependences of logarithmic creep rate with time and strain are observed under transient and tertiary creep. At transient creep, the parameter of $d\ln\dot{\varepsilon}/\varepsilon$ ranges from −150 that is typical for short-term creep [15] to −1100 that is typical for long-term creep of high chromium steels [16]. In contrast to P92 and P93-type steels [7,16,49,52], the present steel exhibits one stage tertiary creep behavior under the long-term creep regime. The creep strength breakdown is characterized by an increase in the $d\ln\dot{\varepsilon}/\varepsilon$ value for the tertiary creep stage from about 50 that is typical for short-term creep [15] to above 100 that is typical for long-term creep [16]. Thus, the transition from short-term to long-term creep is accompanied with an acceleration of kinetics reactions during the transient and tertiary creep stages. The offset strain, ε_{min}, at which the minimum creep rate is attained, varies with the creep regimes (Fig. 2d). The value of ε_{min} decreases by a factor of about 2 with a transition from the short-term creep to long-term one.

The difference between the initial creep rate and the minimum/steady-state creep rate increases with increasing the applied stress. Fig. 3 shows the logarithmic plot of initial creep rate, $\dot{\varepsilon}_{in}$, vs minimum/steady-state creep rate, $\dot{\varepsilon}_{min}$. The plot in Fig. 3 follows a power law [49],

$$\dot{\varepsilon}_{in} = C \cdot \dot{\varepsilon}_{min}^{n}, \tag{6}$$

where M = 0.53 and C = 7.1×10^{-3} are constants. Evidently, an increase in the rupture time with a decrease in the applied stress from 180 to 100 MPa is associated with a decrease in $\dot{\varepsilon}_{min}$ by more than two orders of magnitude, whereas $\dot{\varepsilon}_{in}$ decreases by a factor of 10. Therefore, kinetics processes occurring under transient creep play a key role in the superior creep strength of the steel.

In order to clarify the processes occurring during transient creep, variations of the rate of exhaustion of transient creep, r', vs time to minimum creep rate, t_m, and the minimum/steady-state creep rate, $\dot{\varepsilon}_{min}$, are plotted in Fig. 4a–b. These relationships obey the following power laws.

$$r' \cdot t_m^{1.12} = C_1, \tag{7}$$

and

$$r' \cdot \dot{\varepsilon}_{min}^{-0.79} = C_2, \tag{8}$$

Here, $C_1 = 2.7 \times 10^{-3}$ and $C_2 = 15.5$ are constants. The t_m value increases several orders of magnitude with a decrease in the applied stress from 180 to 100 MPa while the transient strain decreases by a factor of 2.5. Therefore, the stress dependence of minimum/steady-state creep rate is attributed to increasing the offset time. Moreover, decreasing the transient strain in the long-term creep regime raises the role of the offset time in the processes occurring during transient creep. Dependencies of the rate of exhaustion of transient creep and the ε_{min}/t_m parameter on $\dot{\varepsilon}_{min}$ in Fig. 4b–c, respectively, confirm this statement. The increase in the $\dot{\varepsilon}_{in} / \dot{\varepsilon}_{min}$ ratio and postponing the onset of tertiary creep stage are caused by an increase in t_m, increasing the rupture times. Therefore, the processes occurring during transient creep are diffusion-controlled and insensitive to strain. The dependence in Fig. 4c is indicative for the strong correlation between the processes occurring during transient and steady-state creep stages. The linear dependencies of lg r' on lg $\dot{\varepsilon}_{min}$, lg r' on lg t_m, and lg $\dot{\varepsilon}_{in}$ on lg $\dot{\varepsilon}_{min}$ suggest that the transient creep behavior is governed by the first-order kinetics [51]. The creep resistance increases with decreasing the $d\ln\dot{\varepsilon}/\varepsilon$ parameter for the transient creep (Fig. 2c).

It is known [15,53] that at tertiary creep stage, the $d\ln\dot{\varepsilon}/\varepsilon$ parameter

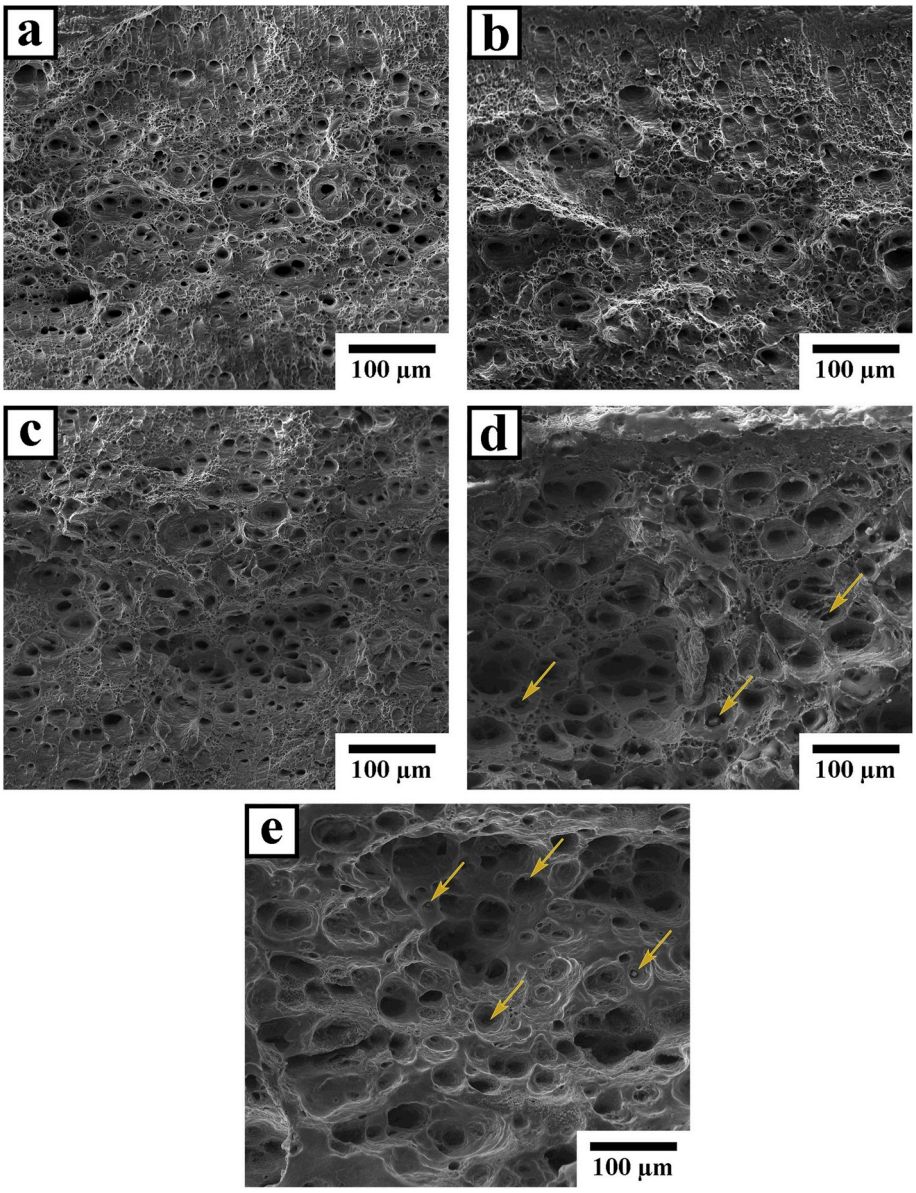

Fig. 7. SEM images of the fractured surfaces after creep tests at 923K for 243 h, 180 MPa (a); 1035 h, 160 MPa (b); 3430 h, 140 MPa (c); 4883 h 118 MPa (d); and 17 863 h, 100 MPa (e). The arrows indicate particles inside dimples.

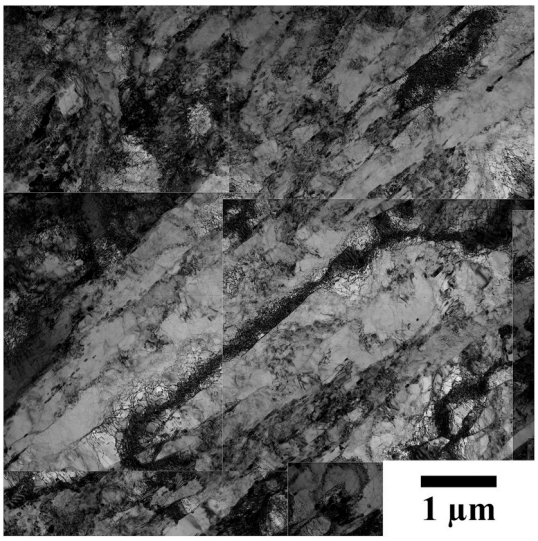

Fig. 8. TEM micrograph showing initial microstructure after tempering at 1023 K.

describes the recovery rate. The variation of the creep strain with time can be expressed by the following relationship [15,53].

$$\varepsilon = \varepsilon_0 + \varepsilon_T[1 - \exp(-r^{'} \cdot t)] + \dot{\varepsilon}_{\min} \cdot t + \varepsilon_3 \exp[p(t - t_r)], \quad (9)$$

Here, ε_3 is the tertiary creep strain and p is the rate of acceleration of tertiary creep evaluated graphically as a slope of the $\ln(\Delta/\varepsilon_3)$ vs $(t\text{-}t_r)$ plot, where $\Delta = \varepsilon - \varepsilon_0 - \varepsilon_T - \dot{\varepsilon}_{\min} \times t_r$ is the tertiary creep component [15,53]. The relationship between p and $\dot{\varepsilon}_{\min}$ obeys the following power law function [53].

$$p \cdot \dot{\varepsilon}_{\min}^{-0.85} = C_3, \quad (10)$$

where $C_3 = 23.4$ is a constant (Fig. 5a). This dependence can be considered as an evidence for the same deformation mechanism controlling both steady-state creep and tertiary creep stages [53].

The dependence between parameter p and the tertiary creep stage duration, $(t_r - t_t)$, where $t_t = t_m$ is the time to the onset of tertiary creep stage, can be expressed as follows (Fig. 5b) [53]:

$$p \cdot (t_r - t_m)^{1.07} = C_4, \quad (11)$$

where $C_4 = 2.4 \times 10^{-3}$ is a constant. A decrease in the rate of acceleration of tertiary creep increases the duration of the tertiary creep stage. After the onset of tertiary creep, the creep rate accelerates to a value of $\dot{\varepsilon}_f = (p \cdot \varepsilon_3 + \dot{\varepsilon}_{\min})$, at which fracture occurs [53]. The dependence of the final creep rate, $\dot{\varepsilon}_f$, on the minimum/steady-state creep rate, $\dot{\varepsilon}_{\min}$, follows (Fig. 5c) [53].

$$\dot{\varepsilon}_f \cdot \dot{\varepsilon}_{\min}^{-0.98} = C_5, \quad (12)$$

where $C_5 = 26.9$ is a constant. The observed dependencies, i.e., Eqs. (10)–(12) in Fig. 5, indicate that the tertiary creep stage obeys the first-order kinetics as the transient creep. Therefore, the physical process at all creep stages are controlled by the first-order kinetics of annihilation and multiplication of dislocations [50,53], although the plot in Fig. 1b suggests that an ability of dislocation to rearrangement by low temperature climb during the long-term creep differs from that during the short-term creep.

3.2. Hardness

Remarkable changes in the hardness in the grip portions of crept specimens occur after aging for more than 5×10^3 h (Fig. 6). The hardness decreases by about 5 and 10% after aging corresponding to the short-term and long-term creep, respectively. Creep leads to pronounced decrease in hardness in the gauge portions of uniform elongation. Hardness after creep for about 10^3 h and that after long-term aging for more than 5×10^3 h are nearly the same. In the range of long-term creep, the hardness tends to decrease with increasing rupture time. The effect of rupture time on hardness near the fracture surface is quite unusual. This hardness increases after short-term creep, or it drops below the level of hardness in the portions of uniform elongation after long-term creep. Thus, there is a clear correlation between the creep strength breakdown and the effect of rupture time on hardness near the fracture surface.

3.3. Fractography

The fracture surfaces of the crept specimens are shown in Fig. 7. The dimple relief suggests prevailing transgranular fracture. An evidence for intergranular cavitation occurring in ductile manner is rarely observed. A number of small dimples with a diameter less than 10 μm is indicative of numerous nucleation sites in the range of short-term creep. Nucleation of larger dimples with an average dimension of about 10 μm are assisted by particles, which are observed on the bottom of dimples, in the range of long-term creep as indicated by arrows in Fig. 7d–e. Markings of serpentine glide can be observed on their walls, indicating considerable plastic deformation upon fracture. Therefore, the formation of coarse particles promotes premature fracture and parameter d in Eq. (2) should depend on parameter m. The fracture is facilitated by the growth of boundary particles in long-term creep regime.

Table 2
The microstructural parameters of the studied steel after creep tests at 923K in different portions of ruptured sample.

	Tempered at 1023K	180 MPa, 243 h		160 MPa, 1035 h		140 MPa, 3430 h		118 MPa, 4883 h		100 MPa, 17863 h		
		Grip portion	3 mm from fracture surface	Grip portion	3 mm from fracture surface	Grip portion	3 mm from fracture surface	Grip portion	3 mm from fracture surface	Grip portion	10 mm from fracture surface	3 mm from fracture surface
Lath/subgrain width, nm	300 ± 20	320 ± 15	565 ± 35	385 ± 20	620 ± 35	405 ± 35	780 ± 55	440 ± 35	910 ± 50	465 ± 30	510 ± 45	1280 ± 115
Dislocation density, × 10^{14} m^{-2}	2.60 ± 0.50	2.25 ± 1.27	1.10 ± 0.35	2.12 ± 0.91	0.45 ± 0.19	1.92 ± 0.62	0.47 ± 0.26	1.20 ± 0.20	0.41 ± 0.26	1.18 ± 0.60	0.40 ± 0.16	0.38 ± 0.15
Average size of $M_{23}C_6$, nm	66 ± 3	74 ± 3	76 ± 4	77 ± 3	86 ± 3	81 ± 3	107 ± 4	93 ± 4	114 ± 8	113 ± 3	142 ± 9	154 ± 11
Average size of $(Fe,Cr)_2(W,Mo)$, nm	–	161 ± 19	165 ± 12	175 ± 13	225 ± 18	256 ± 18	283 ± 18	305 ± 28	367 ± 15	458 ± 40	525 ± 25	550 ± 51
Average size of MX, nm	35 ± 5	35 ± 8	35 ± 7	36 ± 4	38 ± 5	38 ± 7	40 ± 8	38 ± 4	40 ± 5	50 ± 7	52 ± 10	54 ± 7

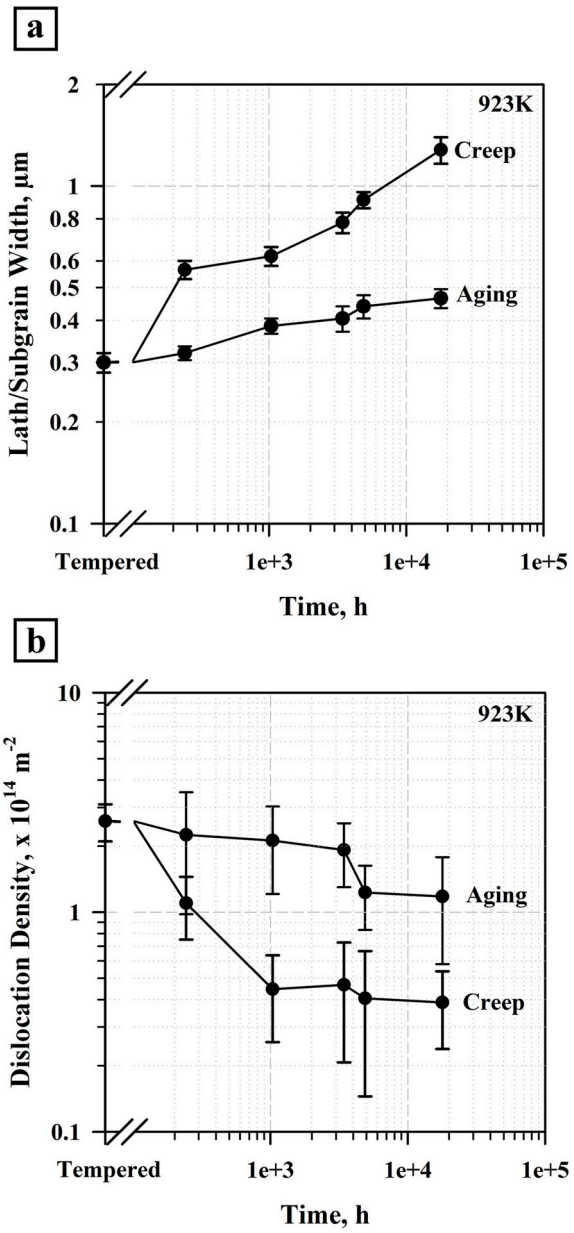

Fig. 9. Lath/subgrain width (a) and dislocation density (b) in the studied steel after creep and aging.

3.4. Evolution of TMLS

The initial microstructure is shown in Fig. 8. This is a typical TMLS with a lath width of 300 nm and a relatively high dislocation density of 2.6×10^{14} m^{-2}. The microstructural parameters including dispersed particles are summarized in Table 2. TMLS remains almost unchanged during long-term aging. The lath dimensions increase by about 50% and the dislocation density decreased by a factor of 2 after aging for 5000 h in comparison with tempered condition (Table 2, Figs. 9 and 10). Further aging does not change TMLS remarkably. The Laves phase precipitations at boundaries of PAGs, packets, blocks and laths after aging for 243 h are clearly visible in Fig. 10 as bright white particles in the SEM images obtained using the Z-contrast technique [15,16]. These particles exhibit an irregular shape and are often located close to $M_{23}C_6$ carbide particles that suggests their nucleation on the $M_{23}C_6$/ferrite interfaces [31,54]. Continuous chains of Laves phase and $M_{23}C_6$ particles appear on HABs of packets and PAGs and semi-continuous chains of these particles evolve along blocks and some lath boundaries. Upon further aging for 17 863 h, coarsening of Laves phase particles leads to increase in their dimension by a factor of above 3 (Figs. 10 and 11, Table 2) while $M_{23}C_6$ carbides increase their dimension by a factor of 2 (Table 2). Remarkable dissolution of Laves phase particles located at lath boundaries is observed after 4883 h aging. After aging for 17 863 h, the lath boundaries are almost free of Laves phase particles. In contrast, a portion of $M_{23}C_6$ carbide particles can be observed on lath boundaries even after long-term aging. The MX carbonitrides are characterized by the lowest coarsening rate among the studied second phase particles (Table 2).

The necking significantly affects TMLS. Typical microstructures of the crept specimens at different distances from the fracture surfaces are shown in Figs. 12–14. Parameters of TMLS and distribution of secondary phase particles in crept specimens are summarized in Table 2 and Fig. 9. The data for subgrain dimensions and/or lath thickness in Fig. 9 and Laves phase dimensions in Fig. 11 were taken in necked areas at 3 mm from the fracture surface. TMLS remains under all applied stresses in the area of uniform elongation of gauge lengths of crept specimens (Fig. 12). However, a decrease in the applied stress leads to an increase in the lath thickness and a decrease in the lattice dislocation density (Table 2). At 100 MPa, the transition from laths to lenticular plate morphology occurs (Fig. 12c). A large portion of initial laths transforms to structural elements with lenticular plate morphology termed as coarse laths [55]. The transformation of lath-type structure to lenticular-type structure promotes the formation of coarse subgrains with round shape in the necked portion of crept specimens (Figs. 9 and 12). The microstructure evolved in the specimen portions close to the fracture surface is typical for the occurrence of continuous dynamic recrystallization (cDRX) [27,56]. Partially recrystallized microstructure with a high portion of grains with average dimension of 5 μm evolves during creep. A decrease in the applied stress leads to an increase in the grains size. It is worth noting that cDRX eliminates Σ3 boundaries with a misorientation of 60.4° (Fig. 12).

The main difference between short-term and long-term creep regimes consists in distribution of boundary particles (Figs. 11, 13 and 14). In the short-term creep regime, the semi-continuous chains of Laves phase particles and $M_{23}C_6$ carbides are observed at almost all boundaries of blocks and some lath boundaries (Fig. 13a, b and 14a). Continuous chains of these particles appear at HABs of packets and PAGs. At 140 MPa, semi-continuous chains of boundary particles were found on some boundaries of blocks, packets and PAGs (Figs. 13c–14b). The coarse subgrains are observed free of $M_{23}C_6$ and Laves phase particles in the necked areas (Fig. 13d). At 100 MPa, the chains of particles are observed on boundaries of PAG, packets and blocks, while the lath boundaries are almost free of any boundary particles (Fig. 13e, f, 14c and 14d). Therefore, at 140 MPa, the coarsening of $M_{23}C_6$ carbides and Laves phase is associated with their partial dissolution at lath boundaries. At 100 MPa, the strain-induced coarsening leads to 30% increase in the dimension of $M_{23}C_6$ carbide particles. Therefore, the creep strength breakdown is associated with the full dissolution of particles on the lath boundaries in the portions of uniform elongation of ruptured specimens. As a result, a number of low-angle boundaries with misorientations ranging from 2 to 5° in gauge lengths can be observed after long-term creep (Fig. 12).

The strain localization accelerates the coarsening of secondary phase particles, especially, $M_{23}C_6$ carbides (Table 2). The strain-induced coarsening of the $M_{23}C_6$ carbide particles is described by growth exponent, N, of 6.1, while $N = 10.5$ is observed for the static coarsening of these particles (Fig. 15a). Moreover, the strain-induced coarsening spreads the size distribution toward large dimensions after creep for 17 863 h (Fig. 15b). Significant portion of relatively coarse carbides with dimensions ranging from 300 to 600 nm appears after creep, while almost all carbides have a size below 300 nm after aging. It has been shown that precipitation of $M_{23}C_6$ carbides takes place during aging and creep up to thermodynamically equilibrium volume fraction [10]. Therefore, two coarsening mechanisms, namely, Ostwald ripening and

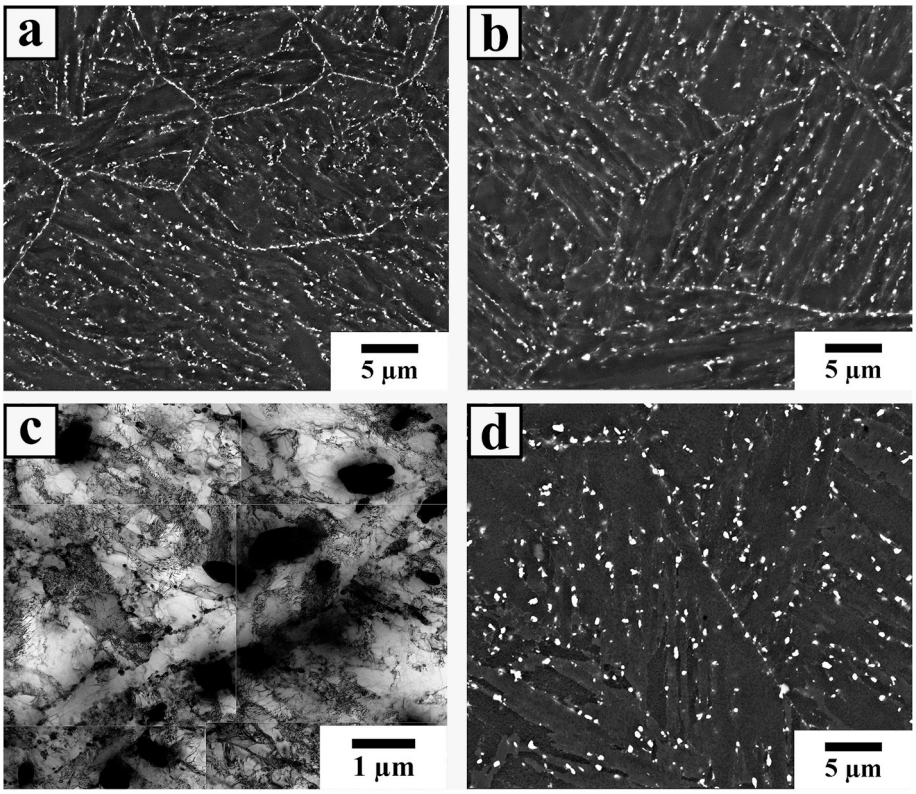

Fig. 10. SEM HAADF (a,b,d) and TEM (c) images showing TMLS decorated by $(Fe,Cr)_2(W,Mo)$ (relatively coarse and bright particles) and $M_{23}C_6$ (fine gray particles) particles after long-term aging for 243 h (a); 3430 h (b); 17 863 h (c,d).

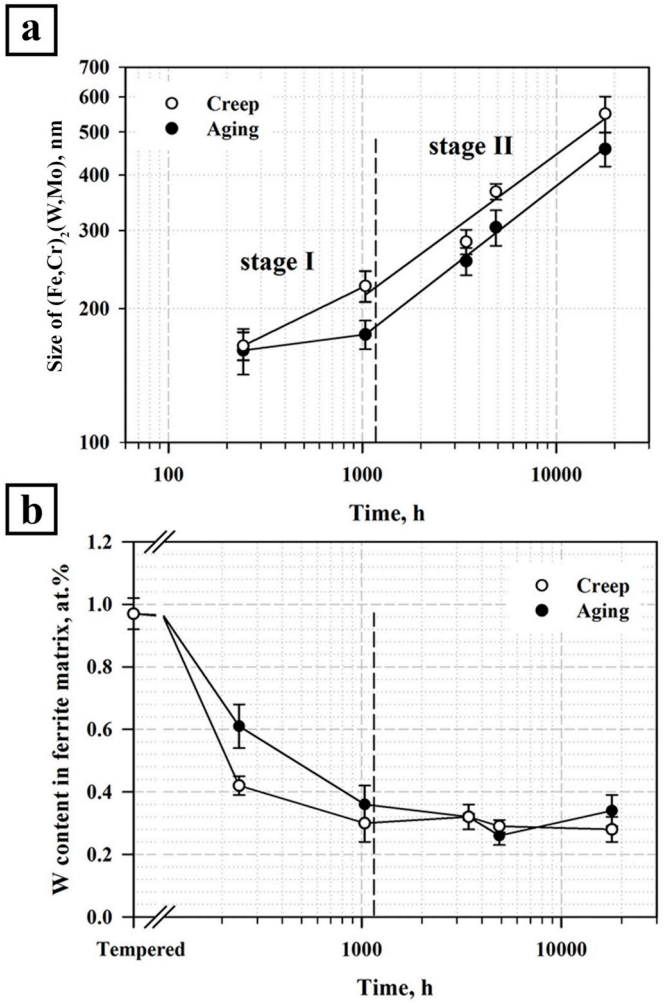

Fig. 11. The coarsening of $(Fe,Cr)_2(W,Mo)$ particles in the studied steel during creep and aging (a) and the change in tungsten content in ferrite matrix during creep and aging (b).

particle growth due to depletion of solid solution, can operate.

TEM investigations revealed the following specific orientation relationships (OR) between the $M_{23}C_6$ carbides and ferrite matrix in the studied steel (Fig. 16).

$(110)_\alpha||(111)_{Cr_{23}C_6}$ $\left[1\bar{1}\bar{1}\right]_{Cr_{23}C_6}$ $\left[1\bar{1}\bar{1}\right]_\alpha||\left[01\bar{1}\right]_{Cr_{23}C_6}$ or Kurdjumov – Sachs OR;

$(110)_\alpha||(111)_{Cr_{23}C_6}$ $\left[00\bar{1}\right]_\alpha||\left[01\bar{1}\right]_\alpha||\left[01\bar{1}\right]_{Cr_{23}C_6}$ or Nishiyama – Wassermann OR;

$(001)_\alpha||(001)_{Cr_{23}C_6}$ $[110]_\alpha||[100]_{Cr_{23}C_6}$ or Brain OR

All these OR are observed in both the aged samples and the areas of uniform elongation of crept specimens. Therefore, original orientation relationships remain almost unchanged during the creep tests.

Most of Laves phase particles precipitate on $M_{23}C_6$/ferrite interfaces that leads to the formation of almost continuous chains of particles on boundaries in short-term creep regime. The Laves phase particles contain mainly Fe, Cr, W and Mo. The W/Mo ratio in these particles is ~2.5, which is close to the nominal ratio of these elements in the steel (Table 1). Coarsening of Laves phase particles leads to the appearance of large particles on boundaries of PAG, packets and within the ferritic matrix as well. An evidence for attractive dislocation–dispersoid interaction was found at the interface boundaries between the matrix and boundary particles. It seems that lattice dislocations attain boundary particles, climb over them and are captured at the detachment side of these particles after the climb has been completed [57]. The growth of $(Fe,Cr)_2(W,Mo)$ particles occurs in two stages (Fig. 11a). The first stage of growth involves continuous precipitation due to depletion of tungsten from ferrite. Deformation accelerates this growth. The strain-induced coarsening of Laves phase particles increases an average size of these particles above 200 μm after creep at 160 MPa. The second stage of Laves phase particle growth is just a coarsening at constant volume fraction also known as Ostwald ripening [58]. At this stage, the strain-induced coarsening is not pronounced. The difference between the particle dimensions after creep and long-term aging is attributed mainly to strain-induced coarsening at first stage.

Long-term creep is accompanied by the two-phase separation of MX-type carbonitrides into Nb-rich and V-rich dispersoids (Fig. 17). In contrast to P92-type steels [28–30], this separation occurs after approx. 10^3 h. It is worth noting that a few particles of Z-phase with the mean particle size of about 70 nm form after creep for 17 863 h (Fig. 18). The (V,Nb)(C,N) carbonitrides are characterized by a relatively high coarsening resistance during both aging and creep (Table 2). Almost the same mean sizes of (V,Nb)(C,N) carbonitrides of 50 nm and 54 nm are observed after aging and creep, respectively, for 17 863 h. Since the size of Z-phase is close to the dimension of MX carbonitrides and the volume fraction of Z-phase is negligible small, the MX→Z-phase transformation is not important for the studied creep strength breakdown.

4. Discussion

4.1. Relationship between creep mechanisms and rupture time

It is known [29,49] that creep strength breakdown in 9%Cr steels is a tertiary creep phenomenon and is associated with downward deviation from the Monkman–Grant relationship [1,29,45,49].

$$t_r = (C_{MG}/\dot{\varepsilon}_{min})^{\alpha}, \quad (13)$$

where C_{MG} is the Monkman–Grant constant and α is a constant being smaller than unity [49,59]. In contrast, the relationship between t_r and $\dot{\varepsilon}_{min}$ observed in the present study follows the Monkman–Grant equation (Fig. 19a). The fracture mechanisms are nearly the same at different creep regimes; and the short-term creep is distinguished from the long-term creep by quantitative characteristics of ductile fracture. Therefore, a decrease in the elongation-to-failure in the range of long-term creep is associated with significant acceleration of tertiary creep stage (Fig. 2b–c). However, the change in power low creep relationship in Fig. 1b suggest that short- and long-term creep differ by creep mechanism operating at steady state. In addition, processes occurring at transient stage are also quite different (see Section 3.1). The first-order kinetic directly related to the microstructure during transient creep affects significantly the steady-state creep behavior [49,50]. Fig. 19b shows the relationship between the offset time, t_m, and $\dot{\varepsilon}_{min}$. Two different linear plots are clearly seen in Fig. 19b. In the range of short-term creep, the t_m vs $\dot{\varepsilon}_{min}$ dependence is stronger by a factor of 2.5 than in the region of long-term creep. The steel is strengthened during the transient creep that decreases $\dot{\varepsilon}_{min}$ and expands the steady-state creep stage. The downward deviation of the $\dot{\varepsilon}_{min}$ vs t_m plot becomes more significant with decreasing the applied stress. Therefore, the transition from short-term creep behavior to long-term one is attributed to changes in the creep mechanisms at all creep stages, i.e., transient, steady-state, and tertiary creep stages.

Relatively high C_{MG} value of 0.257 indicates that the contribution of the offset creep strain to the overall creep strain is rather high. In order to calculate the duration of transient and steady-state creep stages, the apparent region of steady-state creep, $\dot{\varepsilon}_{min} \times t_r$ [15,59], was identified for convenience (Fig. 2a). It is seen that the onset of steady–state appears

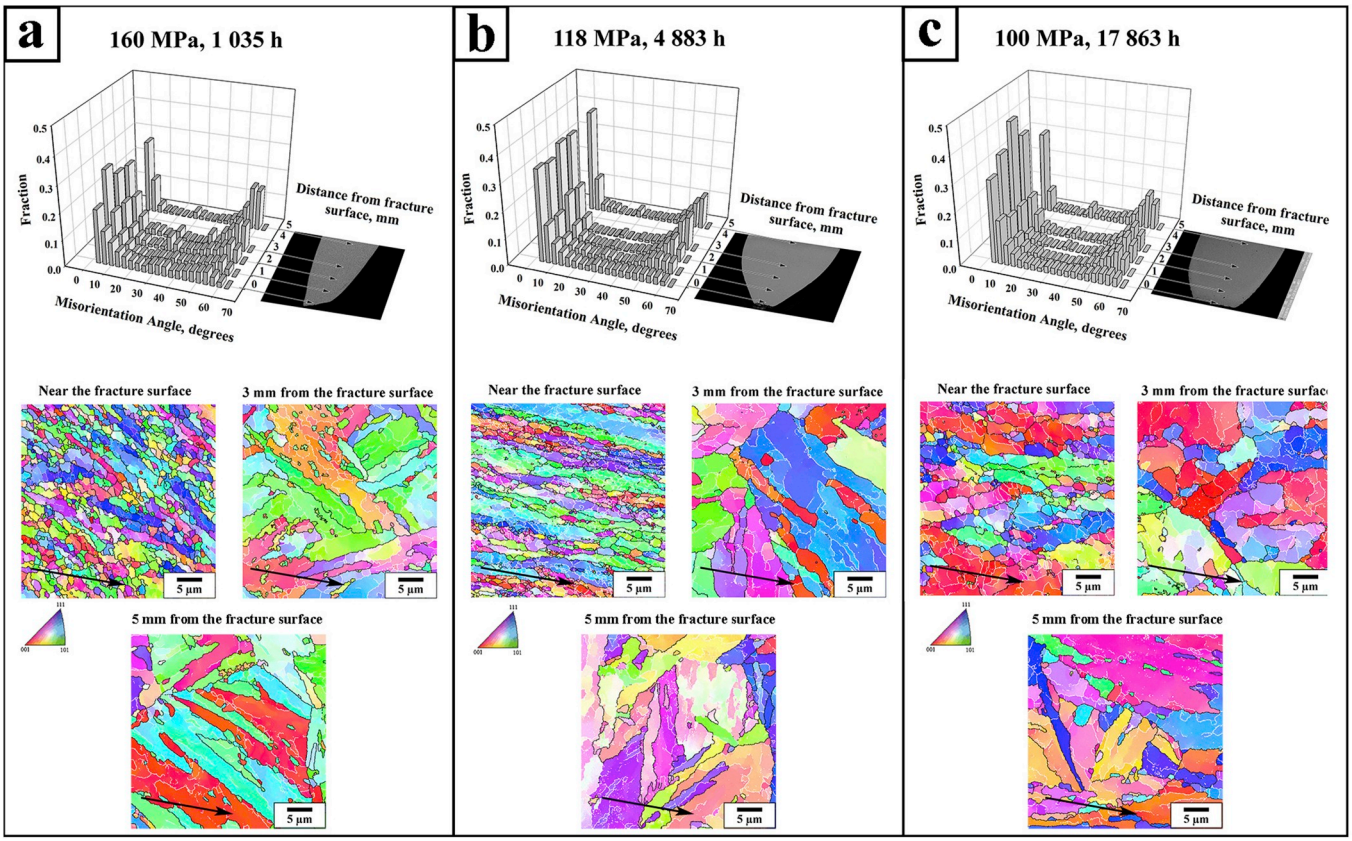

Fig. 12. Microstructures of the studied steel after creep under 160 MPa (a), 118 MPa (b) and 100 MPa (c) evolved at different distances from the fracture surface. The tensile direction is indicated by the arrows.

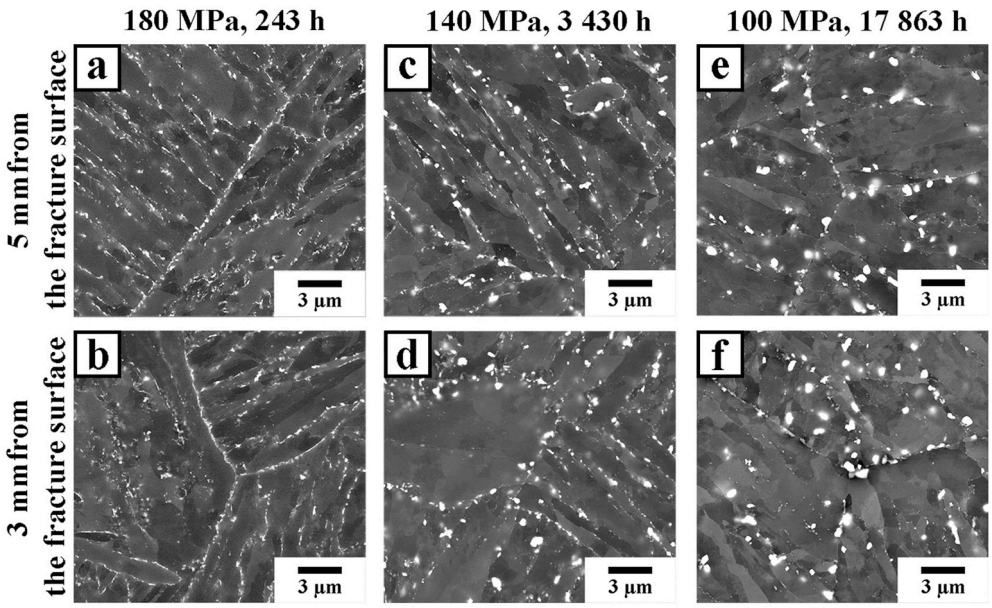

Fig. 13. SEM HAADF images showing $(Fe,Cr)_2(W,Mo)$ and $M_{23}C_6$ particles in ruptured samples crept at applied stress of 180 MPa (a,b), 140 MPa (c,d), and 100 MPa (e,f) in the area of uniform elongation located at least at 5 mm from the fracture surface (a,c,e) and in the necking area located at 3 mm from fracture surface (b,d,f).

at $t < 3{\cdot}10^3$ h even at an applied stress of 100 MPa. In the range of short-term creep, the contribution of tertiary creep to creep life increases with a decrease in the applied stress (Fig. 19c). In contrast, the opposite dependence is observed in the range of long-term creep (Fig. 19c). At low applied stress, the large contribution of the transient and steady-state stages to the creep life compensates acceleration of tertiary creep stage and validates the Monkman–Grant relationship. Thus, the acceleration of softening processes at tertiary creep stage is compensated by strengthening at transient creep stage slowing down the dislocation climb at steady-state creep stage in the long-term creep

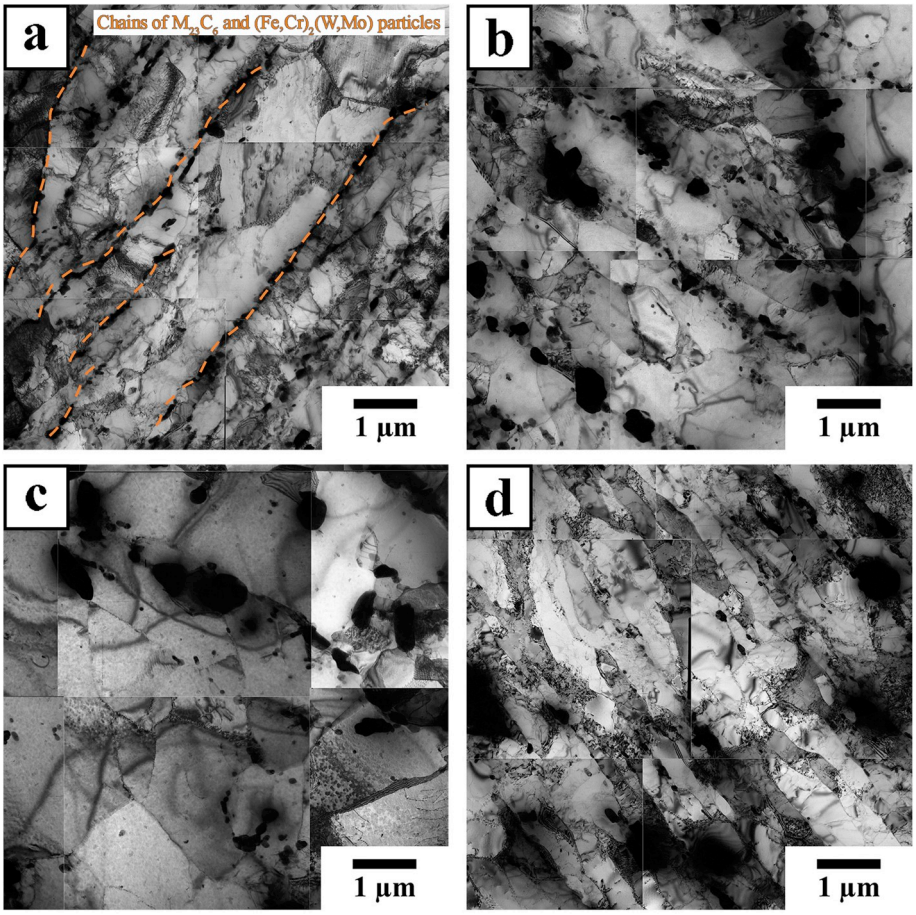

Fig. 14. TEM images of the necked areas located at 3 mm (a,b,c) from fracture surface after creep at applied stress of 180 MPa (a), 140 MPa (b), 100 MPa (c) and in the area of uniform elongation (c) at an applied stress of 100 MPa.

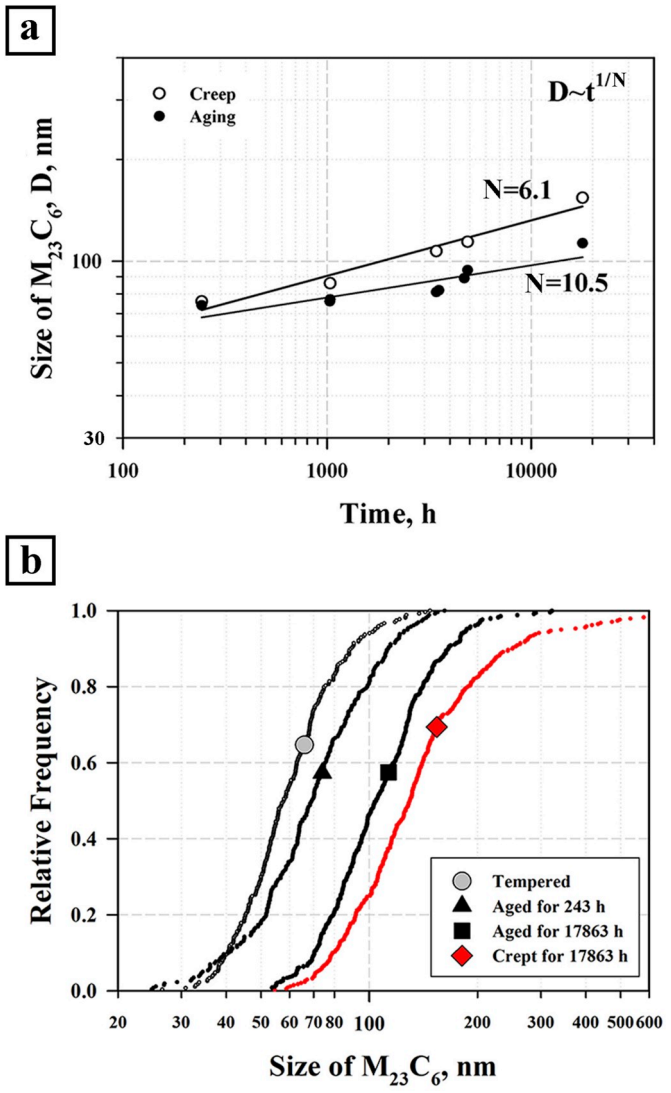

Fig. 15. Effect of time on coarsening of $M_{23}C_6$ carbide particles during creep and long-term aging (a) and the size distribution of $M_{23}C_6$ carbide particles (b).

range (Fig. 2c). As a result, the unified Monkman–Grant relationship describes the t_r *vs* $\dot{\varepsilon}_{min}$ dependence in the whole range of applied stress.

4.2. Creep behavior and a dispersion of secondary phases

The present 9%Cr steel is distinctly different from 10% Cr steels, which do not exhibit the creep strength breakdown up to $4{\cdot}10^4$ h [15,16,19,60] owing to exceptionally high threshold stress [61]. This difference can be attributed to low density of $M_{23}C_6$ carbides precipitated on the lath boundaries during tempering. The precipitation of Laves phase particles at these boundaries during transient creep play a key role in the short-term creep behavior due to increasing the number of obstacles for the dislocation glide along the laths in addition to MX carbonitrides and boundary $M_{23}C_6$ carbides (see Fig. 14 in Ref. [10]). The Laves phase particles precipitated during transient creep remain on the lath boundaries up to rupture. As a result, the dislocation glide occurs along laths on two possible $<111>_{\alpha'}$ directions that is in-lath slip [62,63]. In-lath dislocation slip leads to attractive interaction between a gliding dislocation and Laves phase particles precipitated on lath boundaries [10,25,64]. It has been shown [61] that boundary $M_{23}C_6$ and Laves phase particles give the main contribution to the threshold stress in the 10%Cr steel. In the present 9%Cr steel, the precipitation of Laves phase chains on the lath boundaries during transient creep stage restricts ability of gliding dislocations to rearrangement by climb during short-term creep. Moreover, the lattice dislocations should detach from uniformly distributed MX dispersoids [61]. The boundary particles of Laves phase and matrix MX dispersoids are bypassed by dislocations via a sequential process consisting of local climb, glide of climbing portion of lattice dislocation along the interface boundary and subsequent detachment [57]. Thus, the precipitation of Laves phase particles on lath boundaries is responsible for high stress exponent, n, in the range of short-term creep (Fig. 1b) and the transition from short-term to long-term transient creep behavior (Fig. 2c–d). This type of creep behavior has been attributed to precipitation of Laves phase during transient creep as reported by F. Abe [20] for P9-type steels containing W at $T \leq 600$ °C.

In the region of long-term creep the precipitation of Laves phase and additional VC carbides retard the onset of steady-state creep and decrease the minimum/steady-state creep rate [1,20]. Precipitation of these phases is diffusion-controlled process [33] and, therefore, transient creep is controlled by the appearance of additional obstacles for dislocation glide. However, the onset of rapid coarsening of Laves phase taking place at $\sim 2{\cdot}10^3$ h leads to their full dissolution on the lath boundaries during steady-state creep at 118 MPa [10] or before the onset of steady-state creep at 100 MPa (Figs. 2a and 9). TMLS retains under long-term steady-state creep. The in-lath dislocation gliding overcomes the MX dispersoids by low-temperature climb. This process occurs slowly due to low rate of low-temperature dislocation climb and relatively large size of MX dispersoids. As a result, the long-term steady-state behavior is typical for creep at intermediate temperatures controlled by pipe-diffusion [48]. Thus, the creep strength breakdown is accompanied by the transition from obstacle controlled creep to creep controlled by low temperature climb and the particles located on lath boundaries are extremely important agents for dislocation pinning.

The tertiary creep behavior under long-term creep conditions is characterized by the transformation of TMLS to subgrain structure. This process was termed by K. Maruyama et al. [65] as a strain-induced recovery. In the present 9%Cr steel this transformation occurs in the necked area of crept specimens, only. Therefore, the lath coarsening in the area of uniform elongation accelerates the tertiary creep rate. The transition from lath-type structure to subgrain one in the necked areas leads to a drop in both creep resistance and hardness. The rearrangement of lattice dislocation in subgrains is highly facilitated due to increased length of dislocation line in subgrains. In addition, out-lath dislocation gliding [62,63] under low stresses becomes quite feasible. Sherby et al. [66] have suggested the following relation between the dislocation barrier distance, λ, and steady-state creep rate, $\dot{\varepsilon}_{min}$.

$$\dot{\varepsilon}_{min} \approx \lambda^3, \tag{14}$$

For the short-term creep, the λ value corresponds to the spacing between MX dispersoids of about 180 nm under conditions of short-term creep and the lath thickness of 410 ± 60 nm [10] or the subgrain size of 910 nm for the steady-state creep or tertiary creep, respectively, under conditions of long-term creep. An increase in λ clear correlates with the change in $d \ln\dot{\varepsilon}/\varepsilon$ in Fig. 2c at tertiary creep stage. This significant increase in the λ value contributes to creep rate acceleration during long-term creep. Therefore, transition from short-term to long-term creep is well described by an increase in the λ value controlling the creep rate. The large strains in the necked areas of crept specimens in short-term creep region may promote the DRX development leading to the fine-grained microstructure (Fig. 12a). However, the formation of such microstructure during tertiary creep scarcely affects the creep strength because this microstructure develops right before rupture.

4.3. Precipitation and coarsening of dispersoids

The studied steel is characterized by relatively low coarsening rate of $M_{23}C_6$ carbide particles [10]. The rational orientation relationships remain almost unchanged after long-term ageing and creep in the areas

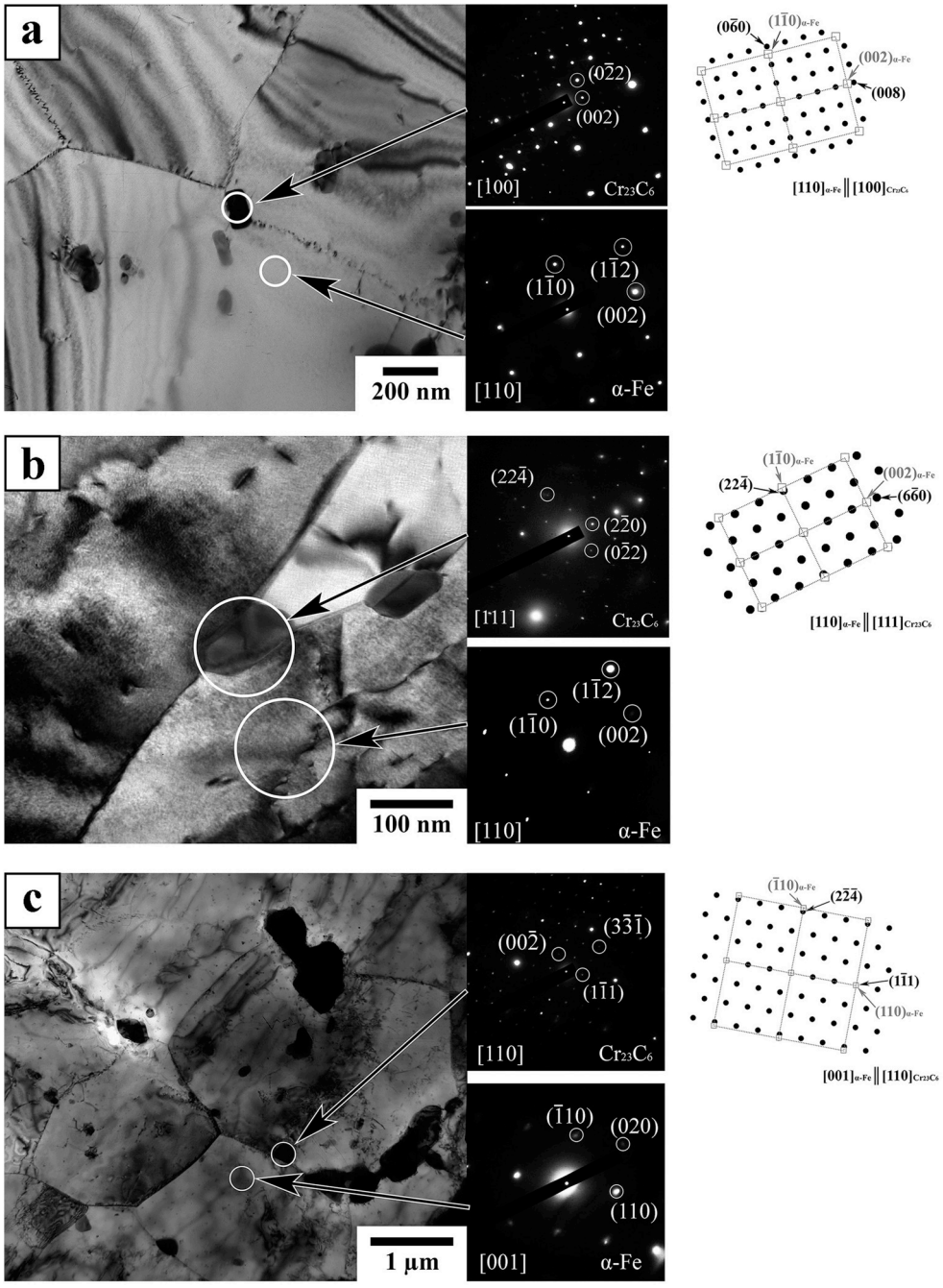

Fig. 16. The observed orientation relationships between $M_{23}C_6$ carbides and ferrite matrix in studied steel: after creep at 140 MPa, 3430 h (a); after aging for 17863 h (b); after creep at 100 MPa, 17863 h (c). The particles in a and c were observed at 3 mm from the fracture surface.

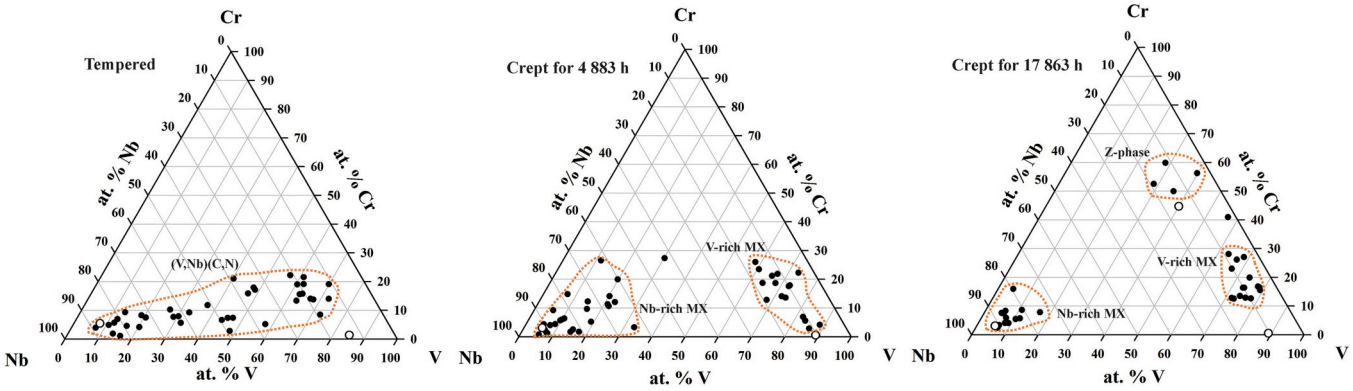

Fig. 17. Change in chemical composition of (V,Nb)(C,N) carbonitrides with increasing the creep time. Open circles represent the calculated equilibrium compositions of Nb(C,N); V(C,N) and Z-phase.

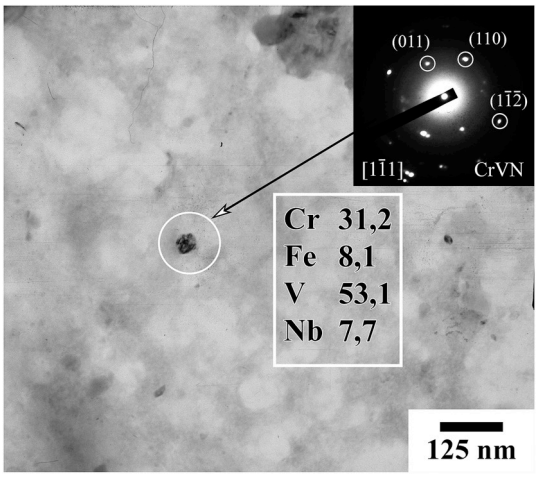

Fig. 18. Z-phase particle after creep for 17 863 h at 923K. The chemical composition is given in at%.

of uniform elongation of ruptured samples (Fig. 16). The presence of two stable carbides (B-free M23C6#1 and B-containing M23C6#2) at tempering and creep temperatures as predicted by ThermoCalc for the studied steel has been reported in previous study [10]. Since these carbides are characterized by similar free Gibbs energy, the small critical size of carbide nuclei and their decreased coarsening rate have been attributed to the decreased interfacial energy of $M_{23}C_6$-type carbides. Another feature of this steel is incomplete precipitation of $M_{23}C_6$ carbides during tempering [10,60]. The boundary $M_{23}C_6$-type carbides precipitated upon tempering act as a collector site for Cr solutes during creep. As a result, precipitation of $M_{23}C_6$ carbides during creep promotes coarsening of existing boundary $M_{23}C_6$ carbides located on PAG and packet boundaries. This process is controlled by fast grain boundary diffusion, leading to significant decrease in overall number density of $M_{23}C_6$ carbides, especially, at the lath boundaries.

The formation of chains of $(Fe,Cr)_2(W,Mo)$ particles along boundaries takes place during aging and transient creep. This process is responsible for unified dependencies between the different parameters of transient creep in short-term and long-term creep regimes (Fig. 4). The size of Laves phase particles exceeds 100 nm even at early stage of their precipitation [10]. Two stage growth of $(Fe,Cr)_2(W,Mo)$ particles can be distinguished (Fig. 17a). The first stage includes continuous precipitation from the ferrite enriched by W and Mo, whereas the second stage consists in Ostwald ripening [58,67]. The latter results in dissolution Laves phase particles located on the lath boundaries. This change in the particle distribution can be responsible for the change in the steady-state creep mechanism and unified dependencies between the different parameters of tertiary creep stage in the whole range of applied stress (Fig. 5).

The (Nb,V)(C,N) carbonitrides, which appear during tempering as non-equilibrium precipitates with a wide range of Nb/V ratios, experience two-phase separation to Nb-rich and V-rich particles during creep. As a result, the MX carbonitrides do not change significantly their size even long-term creep for 17863 h (Table 2). In contrast to P92-type steels with standard nitrogen content of 0.05 wt%, where rapid formation and growth of Z-phase particles lead to dissolution of MX carbonitrides [7,18,35], the present 9%Cr steel with low nitrogen content is characterized by a sluggish kinetics of the formation and growth of

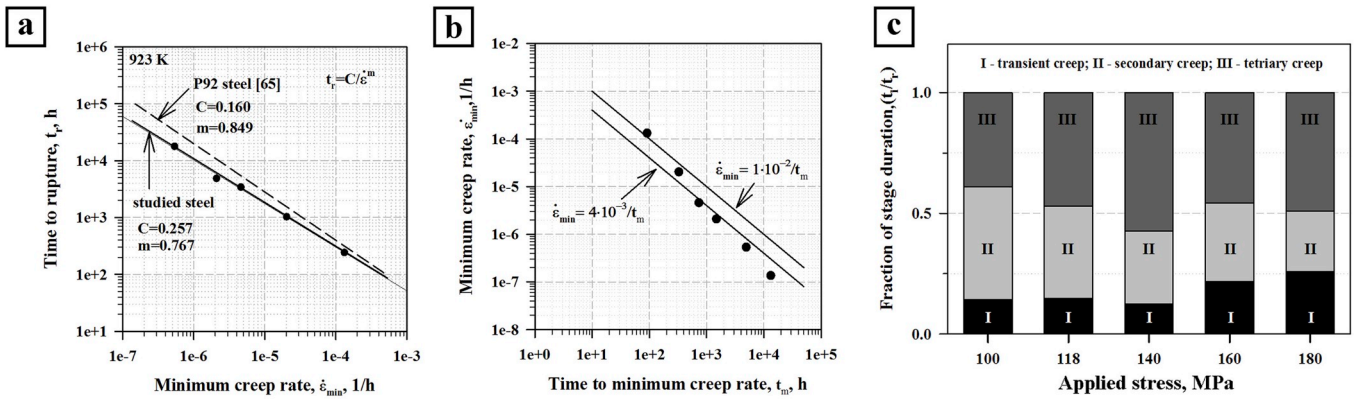

Fig. 19. Relationships between the time to rupture and the steady-state/minimum creep rate (a), and the minimum creep rate normalized by the offset time and the time to minimum creep rate (b). Creep stage durations for the studied steel at an applied stresses of 100–180 MPa (c).

Z-phase. The nanoscale MX and Z-phase dispersoids remain during long-term creep up to the fracture. The creep strength breakdown, therefore, is attributed to the facilitated gliding of lattice dislocations due to the dissolution of particles on lath boundaries and the transformation of TMLS to subgrain one.

5. Conclusions

1. The 9%Cr–3%Co steel with high B and low N contents exhibits the distinct creep strength breakdown at an applied stress of 140 MPa and a rupture time of 3430 h, although the Monkman–Grant relationship is valid in the range of applied stress of 100–180 MPa. The regions of short and long-term creep are distinguished by the creep behavior at all characteristic creep stages, i.e., transient, steady-state and tertiary creep stages. The short-term and long-term creep regimes are characterized by the stress exponent of 13 and 6, respectively, in a power law creep relationship. Transition from the short-term to long-term creep is accompanied with an acceleration of the first order kinetic reactions.
2. Precipitation of Laves phase particles along the lath boundaries results in strengthening during short-term creep. The Laves phase particle coarsening accompanied by their disappearance from the lath boundaries changes the steady-state creep mechanism and increases the rate of tertiary creep under the long-term creep conditions.
3. Numerous precipitations of $M_{23}C_6$ carbides on the lath boundaries is a key factor for superior creep resistance of high Cr steels with high B and low N content.
4. The lath structure remains in the crept specimens in the portions of uniform elongation during the long-term creep, although it transforms to subgrain structure in the necked portions. Under the short-term creep conditions, continuous dynamic recrystallization takes place in the necked area of the crept specimens.
5. The strain-induced formation of Z-phase occurs during the long-term creep. The size of Cr(Nb,V)N nitrides is almost twice in comparison with the size of MX carbonitrides.

Author contribution statement

E. Tkachev: Conceptualization, Methodology, Investigation, Writing - review & editing, A. Belyakov: Validation, Conceptualization, Writing - review & editing, R. Kaibyshev: Project administration, Conceptualization, Writing - original draft.

Acknowledgements

The study was financial supported by the Ministry of Education and Science of Russian Federation, under project of Government Task No. 11.2868.2017/PCh (number for publication 11.2868.2017/4.6). The authors are grateful to the staff of the Joint Research Center, «Technology and Materials», Belgorod State University, for providing the equipment for instrumental analysis.

References

[1] F. Abe, New martensitic steels, in: Mater. Ultra-supercritical Adv. Ultra-supercritical Power Plants, 2016, pp. 323–374, https://doi.org/10.1016/B978-0-08-100552-1.00010-5.
[2] J.S. Lee, H. Ghassemi Armaki, K. Maruyama, T. Muraki, H. Asahi, Causes of breakdown of creep strength in 9Cr-1.8W-0.5Mo-VNb steel, Mater. Sci. Eng. A 428 (2006) 270–275, https://doi.org/10.1016/j.msea.2006.05.010.
[3] W. Bendick, L. Cipolla, J. Gabrel, J. Hald, New ECCC assessment of creep rupture strength for steel grade X10CrMoVNb9-1 (Grade 91), Int. J. Press. Vessel. Pip. 87 (2010) 304–309, https://doi.org/10.1016/j.ijpvp.2010.03.010.
[4] M. Yoshizawa, M. Igarashi, K. Moriguchi, A. Iseda, H.G. Armaki, K. Maruyama, Effect of precipitates on long-term creep deformation properties of P92 and P122 type advanced ferritic steels for USC power plants, Mater. Sci. Eng. A 510–511 (2009) 162–168, https://doi.org/10.1016/j.msea.2008.05.055.
[5] H.G. Armaki, R. Chen, K. Maruyama, M. Igarashi, Creep behavior and degradation of subgrain structures pinned by nanoscale precipitates in strength-enhanced 5 to 12 Pct Cr ferritic steels, Metall. Mater. Trans. A Phys. Metall. Mater. Sci. 42 (2011) 3084–3094, https://doi.org/10.1007/s11661-011-0726-8.
[6] H.G. Armaki, R.P. Chen, K. Maruyama, M. Igarashi, Contribution of recovery mechanisms of microstructure during long-term creep of Gr.91 steels, J. Nucl. Mater. 433 (2013) 23–29, https://doi.org/10.1016/j.jnucmat.2012.09.026.
[7] A. Fedoseeva, N. Dudova, R. Kaibyshev, Creep strength breakdown and microstructure evolution in a 3%Co modified P92 steel, Mater. Sci. Eng. A 654 (2016) 1–12, https://doi.org/10.1016/j.msea.2015.12.027.
[8] A. Kostka, K.G. Tak, R.J. Hellmig, Y. Estrin, G. Eggeler, On the contribution of carbides and micrograin boundaries to the creep strength of tempered martensite ferritic steels, Acta Mater. 55 (2007) 539–550, https://doi.org/10.1016/j.actamat.2006.08.046.
[9] A. Aghajani, C. Somsen, G. Eggeler, On the effect of long-term creep on the microstructure of a 12% chromium tempered martensite ferritic steel, Acta Mater. 57 (2009) 5093–5106, https://doi.org/10.1016/j.actamat.2009.07.010.
[10] E. Tkachev, A. Belyakov, R. Kaibyshev, Creep behavior and microstructural evolution of a 9%Cr steel with high B and low N contents, Mater. Sci. Eng. A 725 (2018) 228–241, https://doi.org/10.1016/j.msea.2018.04.032.
[11] N. Dudova, A. Plotnikova, D. Molodov, A. Belyakov, R. Kaibyshev, Structural changes of tempered martensitic 9%Cr-2%W-3%Co steel during creep at 650°C, Mater. Sci. Eng. A 534 (2012) 632–639, https://doi.org/10.1016/j.msea.2011.12.020.
[12] V. Dudko, A. Belyakov, D. Molodov, R. Kaibyshev, Microstructure evolution and pinning of boundaries by precipitates in a 9 pct Cr heat resistant steel during creep, Metall. Mater. Trans. A Phys. Metall. Mater. Sci. 44 (2013), https://doi.org/10.1007/s11661-011-0899-1.
[13] F. Abe, Analysis of creep rates of tempered martensitic 9%Cr steel based on microstructure evolution, Mater. Sci. Eng. A 510–511 (2009) 64–69, https://doi.org/10.1016/j.msea.2008.04.118.
[14] H. Kitahara, R. Ueji, N. Tsuji, Y. Minamino, Crystallographic features of lath martensite in low-carbon steel, Acta Mater. 54 (2006) 1279–1288, https://doi.org/10.1016/j.actamat.2005.11.001.
[15] R. Mishnev, N. Dudova, A. Fedoseeva, R. Kaibyshev, Microstructural aspects of superior creep resistance of a 10%Cr martensitic steel, Mater. Sci. Eng. A 678 (2016) 178–189, https://doi.org/10.1016/j.msea.2016.09.096.
[16] R. Mishnev, N. Dudova, R. Kaibyshev, On the origin of the superior long-term creep resistance of a 10% Cr steel, Mater. Sci. Eng. A 713 (2018) 161–173, https://doi.org/10.1016/j.msea.2017.12.066.
[17] V. Dudko, A. Belyakov, R. Kaibyshev, Origin of threshold stresses in a P92-type steel, Trans. Indian Inst. Met. 69 (2016) 223–227, https://doi.org/10.1007/s12666-015-0757-8.
[18] A. Fedoseeva, I. Nikitin, N. Dudova, R. Kaibyshev, Strain-induced Z-phase formation in a 9% Cr-3% Co martensitic steel during creep at elevated temperature, Mater. Sci. Eng. A 724 (2018) 29–36, https://doi.org/10.1016/j.msea.2018.03.081.
[19] R. Kaibyshev, R. Mishnev, E. Tkachev, N. Dudova, Effect of Ni and Mn on the creep behaviour of 9-10 %Cr steels with low N and high B, Trans. Indian Inst. Met. 69 (2016) 203–210, https://doi.org/10.1007/s12666-015-0761-z.
[20] F. Abe, Effect of fine precipitation and subsequent coarsening of Fe_2W Laves phase on the creep deformation behavior of tempered martensitic 9Cr-W steels, Metall. Mater. Trans. A 36 (2005) 321–332, https://doi.org/10.1007/s11661-005-0305-y.
[21] H.K. Danielsen, P.E. Di Nunzio, J. Hald, Kinetics of Z-phase precipitation in 9 to 12 pct Cr steels, Metall. Mater. Trans. A Phys. Metall. Mater. Sci. 44 (2013) 2445–2452, https://doi.org/10.1007/s11661-012-1583-9.
[22] L. Cipolla, H.K. Danielsen, D. Venditti, P.E. Di Nunzio, J. Hald, M.A.J. Somers, Conversion of MX nitrides to Z-phase in a martensitic 12% Cr steel, Acta Mater. 58 (2010) 669–679, https://doi.org/10.1016/j.actamat.2009.09.045.
[23] H.K. Danielsen, Review of Z phase precipitation in 9–12 wt-%Cr steels, Mater. Sci. Technol. 32 (2016) 126–137, https://doi.org/10.1179/1743284715Y.0000000066.
[24] R.O. Kaibyshev, V.N. Skorobogatykh, I.A. Shchenkova, Formation of the Z-phase and prospects of martensitic steels with 11% Cr for operation above 590°c, Met. Sci. Heat Treat. (2010) 90–99, https://doi.org/10.1007/s11041-010-9239-0.
[25] V. Dudko, A. Belyakov, R. Kaibyshev, Evolution of lath substructure and internal stresses in a 9% Cr steel during creep, ISIJ Int. 57 (2017) 540–549, https://doi.org/10.2355/isijinternational.ISIJINT-2016-334.
[26] A. Kipelova, R. Kaibyshev, A. Belyakov, D. Molodov, Microstructure evolution in a 3%Co modified P911 heat resistant steel under tempering and creep conditions, Mater. Sci. Eng. A 528 (2011) 1280–1286, https://doi.org/10.1016/j.msea.2010.10.006.
[27] A. Rollett, F. Humphreys, G.S. Rohrer, M. Hatherly, Recrystallization and Related Annealing Phenomena, second ed., 2004, https://doi.org/10.1016/B978-0-08-044164-1.X5000-2.
[28] K. Suzuki, S. Kumai, Y. Toda, H. Kushima, K. Kimura, Two-phase separation of primary MX carbonitride during tempering in creep resistant 9Cr1MoVNb steel, ISIJ Int. 43 (2003) 1089–1094, https://doi.org/10.2355/isijinternational.43.1089.
[29] A. Fedoseeva, N. Dudova, U. Glatzel, R. Kaibyshev, Effect of W on tempering behaviour of a 3 %Co modified P92 steel, J. Mater. Sci. 51 (2016) 9424–9439, https://doi.org/10.1007/s10853-016-0188-x.
[30] I. Fedorova, A. Belyakov, P. Kozlov, V. Skorobogatykh, I. Shenkova, R. Kaibyshev, Laves-phase precipitates in a low-carbon 9% Cr martensitic steel during aging and creep at 923K, Mater. Sci. Eng. A 615 (2014) 153–163, https://doi.org/10.1016/j.msea.2014.07.046.

[31] M.I. Isik, A. Kostka, G. Eggeler, On the nucleation of Laves phase particles during high-temperature exposure and creep of tempered martensite ferritic steels, Acta Mater. 81 (2014) 230–240, https://doi.org/10.1016/j.actamat.2014.08.008.
[32] A. Kipelova, A. Belyakov, R. Kaibyshev, Laves phase evolution in a modified P911 heat resistant steel during creep at 923K, Mater. Sci. Eng. A 532 (2012) 71–77, https://doi.org/10.1016/j.msea.2011.10.064.
[33] D.A. Porter, K.E. Easterling, M.Y. Sherif, Phase Transformations in Metals and Alloys, third ed., 2009, https://doi.org/10.1201/9781439883570.
[34] H. Yu, W. Xu, S. van der Zwaag, On the relationship between the chromium concentration, the Z-phase formation and the creep strength of ferritic-martensitic steels, Steel Res. Int. 89 (2018) 1–8, https://doi.org/10.1002/srin.201800177.
[35] H. Semba, F. Abe, Alloy design and creep strength of advanced 9%Cr USC boiler steels containing high concentration of boron, Energy Mater. 1 (2006) 238–244244, https://doi.org/10.1179/174892406X173611.
[36] F. Abe, M. Tabuchi, S. Tsukamoto, Mechanisms for boron effect on microstructure and creep strength of ferritic power plant steels, Energy Mater. 4 (2012) 166–174, https://doi.org/10.1179/174892312x13269692038851.
[37] R. Sahara, T. Matsunaga, H. Hongo, M. Tabuchi, Theoretical investigation of stabilizing mechanism by boron in body-centered cubic iron through (Fe,Cr)23(C, B)6Precipitates, Metall. Mater. Trans. A Phys. Metall. Mater. Sci. 47 (2016) 2487–2497, https://doi.org/10.1007/s11661-016-3397-7.
[38] F. Abe, Progress in creep-resistant steels for high efficiency coal-fired power plants, J. Press. Vessel Technol. 138 (2016), 040804, https://doi.org/10.1115/1.4032372.
[39] F. Liu, D.H.R. Fors, A. Golpayegani, H.O. Andrén, G. Wahnström, Effect of boron on carbide coarsening at 873 K (600 °c) in 9 to 12 pct chromium steels, Metall. Mater. Trans. A Phys. Metall. Mater. Sci. 43 (2012) 4053–4062, https://doi.org/10.1007/s11661-012-1205-6.
[40] Y.J. Li, D. Ponge, P. Choi, D. Raabe, Segregation of boron at prior austenite grain boundaries in a quenched martensitic steel studied by atom probe tomography, Scr. Mater. 96 (2015) 13–16, https://doi.org/10.1016/j.scriptamat.2014.09.031.
[41] M. Tabuchi, H. Hongo, F. Abe, Creep strength of dissimilar welded joints using high B-9Cr steel for advanced USC boiler, Metall. Mater. Trans. A Phys. Metall. Mater. Sci. 45 (2014) 5068–5075, https://doi.org/10.1007/s11661-014-2471-2.
[42] Y. Liu, S. Tsukamoto, K. Sawada, M. Tabuchi, F. Abe, Precipitation behavior in the heat-affected zone of boron-added 9Cr-3W-3Co steel during post-weld heat treatment and creep deformation, Metall. Mater. Trans. A Phys. Metall. Mater. Sci. 46 (2015) 1843–1854, https://doi.org/10.1007/s11661-015-2802-y.
[43] E. Plesiutschnig, C. Beal, S. Paul, G. Zeiler, C. Sommitsch, Optimised microstructure for increased creep rupture strength of MarBN steels, Mater. High. Temp. 32 (2015) 318–322, https://doi.org/10.1179/0960340914Z.00000000073.
[44] K.G. Abstoss, S. Schmigalla, S. Schultze, P. Mayr, Microstructural changes during creep and aging of a heat resistant MARBN steel and their effect on the electrochemical behaviour, Mater. Sci. Eng. A 743 (2019) 233–242, https://doi.org/10.1016/j.msea.2018.11.075.
[45] B. Xiao, L. Xu, L. Zhao, H. Jing, Y. Han, Deformation-mechanism-based creep model and damage mechanism of G115 steel over a wide stress range, Mater. Sci. Eng. A 743 (2019) 280–293, https://doi.org/10.1016/j.msea.2018.11.083.
[46] B. Xiao, L. Xu, L. Zhao, H. Jing, Y. Han, Y. Zhang, Creep properties, creep deformation behavior, and microstructural evolution of 9Cr-3W-3Co-1CuVNbB martensite ferritic steel, Mater. Sci. Eng. A 711 (2018) 434–447, https://doi.org/10.1016/j.msea.2017.11.061.
[47] K. Kimura, K. Sawada, H. Kushima, K. Kubo, Effect of stress on the creep deformation of ASME Grade P92/T92 steels, Z. Met. Res. Adv. Tech.c 99 (2008) 395–401, https://doi.org/10.3139/146.101651.
[48] O.D. Sherby, P.M. Burke, Mechanical behavior of crystalline solids at elevated temperature, Prog. Mater. Sci. 13 (1968) 323–390, https://doi.org/10.1016/0079-6425(68)90024-8.
[49] F. ABE, Creep behavior, deformation mechanisms, and creep life of Mod.9Cr-1Mo steel, Metall. Mater. Trans. A Phys. Metall. Mater. Sci. 46 (2015) 5610–5625, https://doi.org/10.1007/s11661-015-3144-5.
[50] M.E. Kassner, M.T. Pérez-Prado, Five-power-law creep in single phase metals and alloys, Prog. Mater. Sci. 45 (2000) 1–102, https://doi.org/10.1016/S0079-6425(99)00006-7.
[51] J. Vanaja, K. Laha, M.D. Mathew, Effect of tungsten on primary creep deformation and minimum creep rate of reduced activation ferritic-martensitic steel, Metall. Mater. Trans. A Phys. Metall. Mater. Sci. 45 (2014) 5076–5084, https://doi.org/10.1007/s11661-014-2472-1.
[52] K. Kimura, H. Kushima, K. Sawada, Long-term creep deformation property of modified 9Cr-1Mo steel, Mater. Sci. Eng. A 510–511 (2009) 58–63, https://doi.org/10.1016/j.msea.2008.04.095.
[53] J. Vanaja, K. Laha, Assessment of tungsten content on tertiary creep deformation behavior of reduced activation ferritic–martensitic steel, Metall. Mater. Trans. A Phys. Metall. Mater. Sci. 46 (2015) 4669–4679, https://doi.org/10.1007/s11661-015-3075-1.
[54] M.I. Isik, A. Kostka, V.A. Yardley, K.G. Pradeep, M.J. Duarte, P.P. Choi, D. Raabe, G. Eggeler, The nucleation of Mo-rich Laves phase particles adjacent to M23C6 micrograin boundary carbides in 12% Cr tempered martensite ferritic steels, Acta Mater. 90 (2015) 94–104, https://doi.org/10.1016/j.actamat.2015.01.027.
[55] L. Morsdorf, O. Jeannin, D. Barbier, M. Mitsuhara, D. Raabe, C.C. Tasan, Multiple mechanisms of lath martensite plasticity, Acta Mater. 121 (2016) 202–214, https://doi.org/10.1016/j.actamat.2016.09.006.
[56] T. Sakai, A. Belyakov, R. Kaibyshev, H. Miura, J.J. Jonas, Dynamic and post-dynamic recrystallization under hot, cold and severe plastic deformation conditions, Prog. Mater. Sci. (2014), https://doi.org/10.1016/j.pmatsci.2013.09.002.
[57] R. Kaibyshev, F. Musin, E. Avtokratova, Y. Motohashi, Deformation behavior of a modified 5083 aluminum alloy, Mater. Sci. Eng. A 392 (2005) 373–379, https://doi.org/10.1016/j.msea.2004.10.002.
[58] P.W. Voorhees, The theory of Ostwald ripening, J. Stat. Phys. 38 (1985) 231–252, https://doi.org/10.1007/BF01017860.
[59] B. Xiao, L. Xu, L. Zhao, H. Jing, Y. Han, K. Song, Transient creep behavior of a novel tempered martensite ferritic steel G115, Mater. Sci. Eng. A 716 (2018) 284–295, https://doi.org/10.1016/j.msea.2018.01.047.
[60] I. Fedorova, A. Kostka, E. Tkachev, A. Belyakov, R. Kaibyshev, Tempering behavior of a low nitrogen boron-added 9%Cr steel, Mater. Sci. Eng. A 662 (2016) 443–455, https://doi.org/10.1016/j.msea.2016.03.092.
[61] N. Dudova, R. Mishnev, R. Kaibyshev, Creep behavior of a 10%Cr heat-resistant martensitic steel with low nitrogen and high boron contents at 650 °C, Mater. Sci. Eng. A 766 (2019) 138353, https://doi.org/10.1016/j.msea.2019.138353.
[62] J. Inoue, A. Sadeghi, T. Koseki, Slip band formation at free surface of lath martensite in low carbon steel, Acta Mater. 165 (2019) 129–141, https://doi.org/10.1016/j.actamat.2018.11.026.
[63] H. Na, S. Nambu, M. Ojima, J. Inoue, T. Koseki, Crystallographic and microstructural studies of lath martensitic steel during tensile deformation, Metall. Mater. Trans. A Phys. Metall. Mater. Sci. (2014) 5029–5043, https://doi.org/10.1007/s11661-014-2461-4.
[64] M. Mitsuhara, S. Yamasaki, M. Miake, H. Nakashima, M. Nishida, J. Kusumoto, A. Kanaya, Creep strengthening by lath boundaries in 9Cr ferritic heat-resistant steel, Philos. Mag. Lett. 96 (2016) 76–83, https://doi.org/10.1080/09500839.2016.1154200.
[65] H.G. Armaki, R.P. Chen, K. Maruyama, M. Igarashi, Contribution of recovery mechanisms of microstructure during long-term creep of Gr.91 steels, J. Nucl. Mater. 433 (2013) 23–29, https://doi.org/10.1016/j.jnucmat.2012.09.026.
[66] O.D. Sherby, R.H. Klundt, A.K. Miller, Flow stress, subgrain size, and subgrain stability at elevated temperature, Metall. Trans. A 8 (1977) 843–850, https://doi.org/10.1007/BF02661565.
[67] R.D. Vengrenovitch, On the Ostwald ripening theory, Acta Metall. 30 (1982) 1079–1086, https://doi.org/10.1016/0001-6160(82)90004-9.